Doctoral Thesis

Investigation of high temperature properties of BCC hydrogen storage alloys

Suganthamalar Selvaraj

Graduate School of Integrated Arts and Sciences

Hiroshima University

September 2018

Doctoral Thesis

Investigation of high temperature properties of BCC
hydrogen storage alloys

Suganthamalar Selvaraj

Division of Environmental Science

Graduate School of Integrated Arts and Sciences

Hiroshima University

September 2018

1. Thesis Title

Investigation of high temperature properties of BCC hydrogen storage alloys

2. Research article

1) Study of cyclic performance of V-Ti-Cr alloys employed for hydrogen compressor.

   Suganthamalar Selvaraj, Ankur Jain, Sanjay Kumar, Tengfei Zhang, Shigehito Isobe, Hiroki Miyaoka, Yoshitsugu Kojima, Takayuki Ichikawa.

   International Journal of Hydrogen Energy 43 (2018) 2881-2889.

3. Coauthored article

1) The enhanced de/re‐hydrogenation performance of MgH_2 with TiH_2 additive.

   Mukesh Jangir, Ankur Jain, Shivani Agarwal, Tengfei Zhang, Sanjay Kumar, Suganthamalar Selvaraj, Takayuki Ichikawa, I.P. Jain.

   International Journal of Energy Research 2017, 1-9.

Abstract

The energy demands for the applications and the developing energy systems must be practical, cost-effective, sustainable, reliable and should have a very low impact on the environment. As of now, fossil fuels are being widely used for the energy systems and transportation all over the world. However, the burning of fossil fuel releases a high amount of CO_2 emission which is polluting the air and making global warming. As a solution to this problem, the hydrogen energy technology can be an efficient and suitable technology for the on-board vehicular applications. The development of hydrogen storage material is very important for establishing hydrogen energy infrastructure all over the world in near future. Particularly, the hydrogen storage materials should possess high hydrogen capacity with moderate thermodynamic properties as well as optimum kinetics. Recently, the development of metal hydride compressor is a promising technology for hydrogen compression which has the capability of compressing hydrogen to a high pressure by only increasing heat without the need of any moving mechanical parts.

In this thesis, the hydrogen storage properties and the compressor cyclic performance of V-Ti-Cr BCC alloys were systematically investigated to

understand the effect of high temperature and pressure conditions on their sorption performance.

$V_{20}Ti_{32}Cr_{48}$ and $V_{40}Ti_{21.5}Cr_{38.5}$ two different composition alloys were selected for this study according to their effective hydrogen storage performance. The hydrogen sorption capacity of high vanadium content $V_{40}Ti_{21.5}Cr_{38.5}$ alloy is stable after 10 cycles with their plateau pressures and hysteresis remain almost the same up to 100 cycles. Whereas, low vanadium content $V_{20}Ti_{32}Cr_{48}$ alloy continuously degraded in terms of their hydrogen storage capacity over a number of cycles. Structural and morphological investigations suggest that the low vanadium content alloy have two stable hydride phases i.e $TiH_{0.66}$, and $VH_{0.81}$ after compressor cycling, which requires more than 400 °C to desorb hydrogen completely. This seems to be the responsible reason for the hydrogen storage capacity decrease in each successive cycle of the $V_{20}Ti_{32}Cr_{48}$ alloy.

In order to improve the cyclic and hydrogen storage properties of $V_{40}Ti_{21.5}Cr_{38.5}$ alloy further, the fourth element has been substituted for Cr. Niobium, Iron, and Zirconium elements were selected to alter the thermal stability as well as the cyclic performance of $V_{40}Ti_{21.5}Cr_{38.5}$ ternary alloy at moderate conditions. The $V_{40}Ti_{21.5}Cr_{33.5}Nb_5$ alloy was found stable after 50 cycles of compressor cyclic

test with a higher hydrogen sorption capacity than that of parent and other two alloys. Structural and morphological investigations suggest the formation of $VH_{0.81}$ phase responsible for initial capacity decay for Nb substituted alloy which could not desorb hydrogen at the studied temperature range. The Fe doped $V_{40}Ti_{21.5}Cr_{33.5}Fe_5$ alloy was found continuously degraded over a number of cycles with hydrogen storage capacity. However, structural and morphological investigations suggest no phase segregation during the cycling of $V_{40}Ti_{21.5}Cr_{33.5}Fe_5$ alloy in contrast to the other alloys, which suggest that phase segregation is not the only responsible reason for the performance degradation of BCC alloys employed for compressor cycle. In some cases similar to $V_{40}Ti_{21.5}Cr_{33.5}Fe_5$, stress/strain formation in the lattice during cycling may also cause the degradation of the material. On the other hand, the hydrogen sorption capacity of Zr doped $V_{40}Ti_{21.5}Cr_{33.5}Zr_5$ alloy was found stable after 25 cycles with its plateau pressures and hysteresis remain same up to 100 cycles. The initial degradation was suggested to be associated with the formation of stable hydride phases ZrV_2H_x.

Acknowledgments

First of all, I would like to thanks to God of Almighty for giving strength and wisdom in my entire doctoral course life.

I would like to express my sincere thanks and appreciation to my supervisor, Prof. Dr. Takayuki Ichikawa for his helpful guidance, suggestions, and encouragements throughout the course of this work.

I would like to express my special thanks to my co-advisors Prof. Dr. Norio Ogita, Prof. Dr. Atsuko Namiki, and Assoc. Prof. Dr. Ankur Jain for useful suggestion and discussion for my doctoral thesis.

I am much obliged to Assoc. Prof. Dr. Hiroki Miyaoka and Prof. Dr. Yoshitsugu Kojima for a lot of valuable suggestion and discussion in my doctoral course life.

I would like to express my special thanks to Dr. Sanjay Kumar for his useful suggestion and discussion.

I am very grateful thanks to Prof. Dr. Shigehito Isobe and Dr. Tengfei Zhang in Hokkaido University for performing TEM measurement, analysis of the results,

Contents

List of Figures

1. Introduction

Recently, the development of hydrogen storage and the transportation applications are being studied and developed all over the world to establish an alternative energy infrastructure. This is needed because of the increasing global energy consumption and environmental pollution caused by the present use of fossil fuels [1 - 3]. Essentially, now all the transportation sector is being driven by petroleum fuels, which emit carbon dioxide and nitrogen oxide and enhance pollution on the earth. In addition, a demand has compelled to overcome the depletion of natural resources by renewable-energy based fuels. The attraction of hydrogen as an alternative transportation fuel comes from its clean combust qualities [4].

1.1 Why Hydrogen?

Hydrogen is the first element in the periodic table having atomic number 1 (1 electron, 1 proton) and the electron configuration $1s^1$. Hydrogen is the most abundant element in the universe (75% of the mass) and is simplest, lightest, non-polluting, environmentally friendly, highly volatile and nontoxic gas [5]. On the earth, less than 1.0% of molecular hydrogen gas exists in the air, but a huge amount of hydrogen is available in the chemically bounded form in H_2O

as well as in hydrocarbons. Hydrogen has the highest gravimetric energy density per unit of weight among all the chemical fuels (~2-3 times more efficient than gasoline vehicles), but the lowest energy content by volume [6]. In addition, it is considered as pollution-free fuel because when it is burnt with oxygen, only water is exhausted.

Especially hydrogen is expected to be used as automobile fuel instead of gasoline because hydrogen energy can easily be converted into electric energy by using a fuel cell. There are two ways of using hydrogen for the vehicle, one is hydrogen as an internal combustion engine in vehicles and is burnt rapidly with oxygen from the air. Second is hydrogen burnt with oxygen from the air in the fuel cell electrochemically, which produces the electricity to drives the fuel cell electric vehicle [7].

Hydrogen is a secondary energy source which is produced from the supply of primary energy resources without any pollution such as solar power, wind power, hydroelectric, and ocean energy.

1.2 Hydrogen Storage Technologies

Since the density of hydrogen is very less, it need to be stored efficiently. Except this it is easy to explode if not handled properly and carefully. Thus according to these requirements, hydrogen can be stored in 3 different forms namely: compressed, cryogenic and solid state materials. This section presents brief description about all the three methods:

1.2.1 Compressed storage

At ambient temperature (25°C), hydrogen gas is described by the Van der Waals equation:

$$\left(p + a\frac{n^2}{V^2}\right)(V - nb) = nRT \tag{1.1}$$

where p is the gas pressure, V the volume, T the absolute temperature, n the number of moles, R the gas constant ($R = 8.314$ J K^{-1} mol^{-1}), a is the dipole interaction or repulsion constant ($a = 2.476 \times 10^{-2}$ m^6 Pa mol^{-2}), and b is the volume occupied by the hydrogen molecules ($b = 2.661 \times 10^{-5}$ m^3 mol^{-1}) [1-8].

The Virial Expansion

The virial expansion, also called the virial equation of state, is the most interesting and versatile of the equations of state for gases. The virial expansion is a power series in powers of the variable, *n/V,* and has the form,

$$\frac{pV}{nRT} = Z = 1 + B(T)\frac{n}{V} + C(T)\frac{n^2}{V^2} + \cdots \infty \qquad (1.2)$$

The coefficient, $B(T)$, is a function of temperature and is called the "second virial coefficient". $C(T)$ is called the third virial coefficient, and so on. The expansion is, in principle, an infinite series, and as such should be valid for all isotropic substances. In practice, however, terms above the third virial coefficient are rarely used in chemical thermodynamics.

Notice that we have set the quantity pV/nRT equal to Z. This quantity (Z) is called the "compression factor." It is a useful measure of the deviation of a real gas from an ideal gas. For an ideal gas, the compression factor is equal to 1.

The Boyle Temperature

The second virial coefficient, $B(T)$, is an increasing function of temperature throughout most of the useful temperature range. (It does decrease slightly at very high temperatures.) B is negative at low temperatures, passes through zero at the so-called "Boyle temperature," and then becomes positive. The temperature at which $B(T) = 0$ is called the Boyle temperature because the gas obeys Boyle's law to high accuracy at this temperature. We can see this by noting that at the Boyle temperature the virial expansion looks like,

$$\frac{pV}{nRT} = 1 + 0 + C\frac{n^2}{V^2} + \cdots \infty \tag{1.3}$$

If the density is not too high the C term is very small so that the system obeys Boyle's law.

Alternate form of the virial expansion

An equivalent form of the virial expansion is an infinite series in powers of the pressure.

$$\frac{pV}{nRT} = 1 + B'(T)p + C''(T)p^2 + \cdots \infty \tag{1.4}$$

The new virial coefficients, B', C'', . . . , can be calculated from the original virial coefficients, B, C, ... To do this we equate the two virial expansions,

$$\frac{pV}{nRT} = 1 + B(T)\frac{n}{V} + C(T)\frac{n^2}{V^2} + \cdots \infty$$

$$= 1 + B'(T)p + C''(T)p^2 + \cdots \infty \tag{1.5}$$

Then we solve the original virial expansion for p,

$$p = \frac{nRT}{V}\left(1 + B(T)\frac{n}{V} + C(T)\frac{n^2}{V^2}\right) + \cdots \infty \tag{1.6}$$

and substitute this expression for p into the right-hand-side of equation *(1.5)*,

$$1 + B\frac{n}{V} + C\frac{n^2}{V^2} + \cdots$$

$$= 1 + B'\frac{nRT}{V}\left(1 + B\frac{n}{V} + C\frac{n^2}{V^2} + \cdots\right)$$

$$+ C''\left(\frac{nRT}{V}\right)^2\left(1 + B\frac{n}{V} + C\frac{n^2}{V^2} + \cdots\right)^2 + \cdots \tag{1.7a}$$

$$1 + B\frac{n}{V} + C\frac{n^2}{V^2} + \cdots = 1 + B'RT\frac{n}{V} + B'RTB\frac{n^2}{V^2}\cdots +$$

$$C''(RT)^2\frac{n^2}{V^2} + \cdots \tag{1.7b}$$

Both sides of Equation *(1.7b)* are power series in *n/V*. (We have omitted third and higher powers of *n/V* because the second power is as high as we are going here.) Since the two power series must be equal, the coefficients of each power of *n/V* must be the same on both sides. The coefficient of $(n/V)^0$ on each side is 1, which gives the reassuring but not very interesting result, $1 = 1$.

Equating the coefficient of $(n/V)^1$ on each side gives $B = B'RT$ and equating the coefficients of $(n/V)^2$ gives

$$C' = B'RTB + C''(RT)^2 \qquad (1.8)$$

These equations are easily solved to give B' and C' in terms of B, C, and R.

$$B' = \frac{B}{RT} \qquad (1.9)$$

$$C'' = \frac{C' - B^2}{(RT)^2} \qquad (1.10)$$

The virial coefficients can be calculated from a theoretical model of the intermolecular potential energy of the gas molecules [9].

In this type, hydrogen is stored in a conventional high-pressure gas cylinder with high gravimetric and acceptable volumetric density. The most common

storage systems have a maximum pressure of 20MPa. Recently, 70MPa high-pressure tanks have also been developed for fuel cell vehicles with 110 kg mass, gravimetric density 6.0 mass% and volumetric density 30 kg m^{-3}. However, the compression itself is the most dangerous and complicated technique. The gravimetric density of hydrogen in a loaded pressure cylinder depends on the material and mass of the cylinder. The volumetric density of hydrogen increases with pressure reaches a maximum. Therefore, for the production of the cylinder, material is important. Recently, new lightweight carbon composite cylinders made with a high molecular weight polymer or aluminum liner [10-12] have been developed to support pressure up to 80MPa, therefore the hydrogen reaches a volumetric density of 36 kg m^{-3} compared with the cylinders made of iron [13].

1.2.2 Cryogenic storage

In this type, hydrogen is stored as a liquid form in a cryogenic container at around -253°C under normal pressure with a high volumetric density of 70.8 kg m^{-3} which makes it a better option than that of the hydrogen gas due to which liquid hydrogen has been widely used as a fuel in space technology. It also has the best and highest energy-to-weight ratio of all the fuels. However, it requires

a large amount of energy to liquefy the hydrogen gas (currently 10 kWh kg^{-1}H$_2$ which is 25% of the total energy of H$_2$). In addition, the thermal insulation of the cryogenic storage vessel is needed in order to reduce the boil-off of hydrogen. This is one of the problems concerning the use of liquid hydrogen. The liquefaction and to limits the continuous boil-off hydrogen need a large amount of energy for hydrogen storage system [13, 14]. Most liquid hydrogen tanks are spherical because this shape has the lowest surface area for heat transfer per unit volume. As the diameter of the tank increases, the volume increases faster than the surface area, so a large tank will have proportionally less heat transfer area than a small tank, reducing boil-off. Cylindrical tanks are sometimes used because they are easier and cheaper to construct than spherical tanks and their volume-to-surface area ratio is almost the same [15].

1.2.3 Hydrogen in solid state materials

In this type, hydrogen can be stored safely in solid state materials and it has higher gravimetric and volumetric density of hydrogen as compared to the gaseous and liquid hydrogen storage systems [6]. Recently, several kinds of materials have been studied for storing hydrogen in the form of their hydrides. Some hydrides can desorb hydrogen at room temperature and atmospheric

pressure, while others require very high temperature for hydrogen desorption. These systems could be used for onboard and other stationary application. The required material properties for hydrogen storage should be:

1. High volumetric and gravimetric hydrogen density.
2. The reversible hydrogen absorption/desorption under suitable thermodynamics properties of moderate temperature and pressure.
3. Fast Kinetics.
4. Easy handling.
5. Low cost and abundant resources.

The types of hydrogen sorption for hydrogen storage materials can be classified on the basis of the sorption process, which is physisorption and/or chemisorption. Physisorption hydrogen storage materials can absorb hydrogen only on the surface of the solid via the interaction of hydrogen molecules with several atoms at the surface of a solid. The potential energy of the hydrogen molecule is approximately one molecular radius of the adsorbate. Physisorption is only observed at low temperatures because of the Van der Waals interaction [14]. Chemisorption hydrogen storage materials are metallic and chemical hydrides. Volumetric density of this system is generally higher than that of the

physisorption, gaseous and liquid hydrogen storage systems. Further development of this system is important for the onboard application [15].

1.3   Solid state hydrogen storage

1.3.1 Metal hydrides

Many metals, intermetallic compounds, and alloys, in general, react with hydrogen and form mainly solid-metal hydrogen compounds. When hydrogen is exposed to metal at certain pressures and temperatures, metal absorbs large quantities of the gas and forms metal hydride compounds. When absorption is started into the metal, hydrogen is distributed compactly throughout the metal lattice. The hydrogen can be desorbed (released) as a gas by altering the temperature and pressure and the metal is returned back to its original state. The metal hydride forms through a metallic bond and the other hydrides are formed through various kinds of the bonds such as a covalent bond, ionic bond, and hydrogen bond. Metal hydrides represent an exciting method for storing hydrogen and it is inherently safer than compressed gas or liquid hydrogen and has a higher volumetric hydrogen storage capacity [16].

Many metals can form metal hydrides, a typical reaction can be expressed as

$$M + H_2 \leftrightarrow MH_2 \qquad\qquad (1.11)$$

Where, M represents the metal and H is hydrogen.

The detailed knowledge of metal hydride is very important for the development of solid-state hydrogen storage units for fuel cells and other devices. Recently, several developments on metal hydrides have been taken place in order to improve their properties including hydrogen storage capacity, kinetics, cyclic behavior, toxicity, pressure and the thermal response which are needed for the future transportation and the development in hydrogen economy [17].

1.3.2 Types and family of Metallic hydrides

The alloys can be designed by the combination of the strong hydriding elements A with non-hydriding B metals which can achieve desirable pressure composition temperature (PCT) properties (detailed information is in section 3.2.5) of excellent and reversible hydrogen absorption and desorption properties. Generally, the alloys are written like AB_5, AB_2, AB_3, A_2B_7, A_6B_{23}, AB, and A_2B, where, the hydride-forming component is generally among Mg, Ca, IIIB, IVB, VB elements and the non-hydride-forming component B is from VIB, VIIB,

VIII groups as shown in Fig 1.1. The structure of all these intermetallic compounds and their hydrides are described in Table 1.1. [1].

Table 1.1 The most important families of hydride-forming intermetallic compounds including the prototype and the structure

A is an element with a high affinity to hydrogen and B is an element with a low affinity to hydrogen.

Intermetallic compound	Example		Structure	Capacity (wt %)
	Alloys	**Hydrides**		
AB_5	$LaNi_5$	$LaNiH_6$	Haucke phases, hexagonal	1.4
AB_2	ZrV_2	$ZrV_2H_{5.5}$	Laves phase, hexagonal or cubic	3.0
AB_3	$CeNi_3$	$CeNi_3H_4$	Hexagonal, $PuNi_3$-type	1.8
A_2B_7	Y_2Ni_7	$Y_2Ni_7H_3$	Hexagonal, Ce_2Ni_7-type	0.5
A_6B_{23}	Y_6Fe_{23}	$Y_6Fe_{23}H_{12}$	Cubic, Th_6Mn_{23}-type	0.7
AB	$TiFe$	$TiFeH_2$	Cubic, CsCl or CrB-type	1.9
A_2B	Mg_2Ni	Mg_2NiH_4	Cubic, $MoSi_2$ or Ti_2Ni-type	3.6

1.4 Thermodynamics of Metal-Hydrogen System

In order to design the energy exchanges involved in the formation of a metal-hydrogen alloy or compound for practical use, and a knowledge of the energy state of that alloy or compound is necessary for the scientific approach to the subject of metal-hydrogen systems. A successful solid-state reversible storage material should meet the requirements of high storage capacity, suitable thermodynamics properties, reversibility and fast kinetics absorption and desorption kinetics. Thermodynamics plays an important role in the implementation of a metal-hydrogen system to the practical applications. The high stability of metal hydrides requires high operating temperature, which is one of the important challenges to be solved [18-21].

The hydrogen gas reacts with many transition metal to form hydrides. Initially, hydrogen gas molecule potentials and of two hydrogen atoms are separated by the dissociation energy ($H_2 \rightarrow 2H$, $E_D = 435.99$ kJ mol^{-1} H_2) [1]. The hydrogen molecule approaching the metal surface is under van der Waals force and leads to the physisorbed state ($E_{phys} < 10$ kJ mol^{-1} H_2). Secondly, the dissociated hydrogen atoms closer to the surface has to overcome an activation barrier for the formation of hydrogen metal bond. Hydrogen atoms share their electron

with the metal atoms at the surface, which leads to the formation of a chemisorbed state ($E_{chem} > 50$ kJ mol^{-1} H$_2$). In the next step, the chemisorbed hydrogen atom jump in the subsurface layer and diffuse on the interstitial sites through the host metal lattice. The hydrogen absorption process can be described in terms of a simplified one-dimensional potential energy curve as shown in Fig. 1.2 [22].

The thermodynamic aspects of hydride formation from gaseous hydrogen are described by means of pressure-composition isotherms (PCI) as shown in Fig 1.3(a), the detailed methodology of these isotherms would be described in section 3.2.5. With increasing pressure of hydrogen gas at low concentration region, a solid solution of hydrogen into metal lattice starts to form which is denoted as α phase. For a dilute solid solution, the relation between hydrogen gas pressure and hydrogen concentration is described by the Hendry-Sieverts law as follows [23].

$$C_H = K_S \sqrt{P} \qquad (1.12)$$

Where, K_S is Sievert's constant, P hydrogen pressure, C_H hydrogen concentration in the metal. This equation indicates that the hydrogen concentration increases in proportional to the square root of hydrogen pressure

in the low concentration region. When the maximum solubility of hydrogen in the α phase is reached, the formation of hydride β-phase starts to grow by the hydrogen occupation of particular interstitial sites. In the equilibrium condition, the hydrogen pressure remains constant even though hydrogen is continuously absorbed with increasing in the hydride phase (β-phase). The relation between the phases, components, and degree of freedom for the metal-hydrogen system could be represented by usual thermodynamics relation of the Gibbs phase rule as below [24].

$$F = C-P+2 \tag{1.13}$$

Where, F is the degree of freedom, P is the number of phases and C is the number of chemical components. Here the component is always 2 i.e. metal and H_2 gas. In the plateau region, no. of phases are 3 i.e. α phase, β phase, and gaseous hydrogen which gives a degree of freedom (F) as 1. Therefore, in the isothermal condition, the hydrogen concentration increased at a constant hydrogen pressure, which is generally called the plateau (equilibrium) pressure P_{eq}. After reaching to saturation, further addition of hydrogen increase the pressure and form β phase region of PCT diagram as shown in Fig 1.3(a) [25].

The plateau pressure is increased with increasing temperature with decreasing plateau width and vanish completely when it reaches the critical temperature.

The Plateau pressure region gives the very important information required for hydrogen storage application, for instance, the reversible hydrogen storage capacity can be estimated from the width of the plateau, whereas the position of the plateau pressure at a given temperature may give an idea of the stability of the hydride. The stable hydride requires a higher temperature than less stable hydrides to reach a certain plateau pressure.

Hydrogen absorption and desorption reaction to form metal hydride phase or the solid solution is an exothermic and endothermic process respectively. The enthalpy (ΔH) and entropy (ΔS) of formation are defined as the difference in the stability between α and β phases. This can be directly estimated from the set of equilibrium PCI measurement at a different temperature as shown in Fig 1.3(a) [26-27].

The thermodynamic properties can be described by van't Hoff equation

$$\ln(P_{eq}/P^0) = \Delta H/RT - \Delta S/R \tag{1.14}$$

The change in the enthalpy and entropy of reaction can be experimentally obtained from the van't Hoff plot, slope and intercept of $\ln(P_{eq}/P^0)$ versus $1/T$, as shown in Fig 1.3(b).

The standard enthalpy of metal-hydrogen systems capable to work at ambient condition can be calculated as follows,

According to Eq. 1.14

$$\ln 1 = \frac{\Delta H}{8.314 \times 300} + \frac{130}{8.314}$$

$$\Delta H = -39 \text{ kJ mol}^{-1} \text{ H}_2$$

Where, the ambient conditions are: pressure P_{eq} = 0.1MPa; P^0=1 atm; temperature T = 300K, the gas constant R = 8.314 J K^{-1} mol^{-1} and the entropy of hydride formation is equal to standard entropy of hydrogen gas i.e. ΔS = -130 JK^{-1} mol^{-1}H$_2$.

The stability of metal hydrides is usually presented in the form of van't Hoff plots according to Eq.(1.14) and are shown in Figure.1.4 for selected hydride systems.

1.5 Metal hydride for hydrogen compressor

Several mechanical compressors are commercially available such as an electrochemical compressor, ionic liquid piston compressors. However, they are noisy and have many complications and difficulties in their operation. The hydrogen embrittlement is one of the main issues associated with these mechanical compressors which is expressed as undesirable effects due to hydrogen such as loss of ductility, decreased fracture toughness, and degradation of fatigue properties of metals [28]. Metal hydride hydrogen compressor has been considered as a potential application, an efficient and reliable method for hydrogen energy systems which utilize reversible heat driven interaction of hydrogen with metal, alloy, or intermetallic compound to form a metal hydride. Metal hydride hydrogen compressor has high volumetric density without any moving part, so they provide a safe, compact, simple, and reliable option [30]. Hydride compressor uses metal hydrides with low-pressure hydrogen gas absorption at ambient temperature and desorption of high-pressure hydrogen gas at a higher temperature as shown in Fig 1.5 [29].

1.6 V-based BCC alloys

In order to realize metal hydride compressor, the material should possess several properties including high reversible hydrogen content, Fast kinetics, low plateau slope, low hysteresis, suitable overall PCT properties [31]. To achieve these properties numerous efforts have been made and several materials are developed so far. Among them, V based BCC materials have attracted the scientific community to develop hydrogen compressor [32-33] owing to their high hydrogen capacity and favorable thermodynamic properties [15, 34, 35]. Vanadium forms two hydrides [30], VH_{1-x} and VH_{2-x} where the transition between the mono- and dihydride is characterised by a reversible hydrogen storage capacity of about 1.9 wt.% H at near-ambient conditions and has a steep temperature dependence of hydrogen equilibrium pressure, associated with unusually high values of entropy and enthalpy of the formation of vanadium dihydride. Due to this reason, the BCC vanadium alloys are attractive candidates for the metal hydride hydrogen compressors. The introduction of Ti in vanadium makes it suitable for compressor application in terms of their hydrogenation properties [36-45]. The addition of Chromium with Ti-V system improves the cyclic stability and the resistance of material towards pulverization without affecting the effective H_2 storage capacity [46-49]. Till

date, several Ti-Cr-V alloys have been studied for their structural, hydrogenation and cyclic properties. The $V_{60}Ti_{15}Cr_{25}$ alloy has been found to have the highest effective capacity of 2.62 wt% out of several studied combinations [50]. The cyclic durability of $V_{40}Ti_{24}Cr_{36}$ alloy has been examined and it was found quite stable up to 100 cycles with absorption and desorption plateau pressure at around 0.1 and 0.04 MPa, respectively [51]. In another work, $V_{20}Ti_{32}Cr_{48}$ alloy has shown 2.4~2.5 wt% desorption capacity with absorption/desorption plateau pressure at around 0.3 and 0.09 MPa at 313 K [52, 53]. During hydrogen absorption and desorption, TiH_2 hydride phase appeared for TiCrV and $Ti_{0.8}Cr_{1.2}V$ alloys which reduce the cyclic hydrogen capacity [54]. It is interesting to note that the activation have been found difficult for high vanadium content alloys, whereas poor cyclability has been observed for low vanadium content alloys.

Figures

Figure 1.1: Periodic table of the Elements
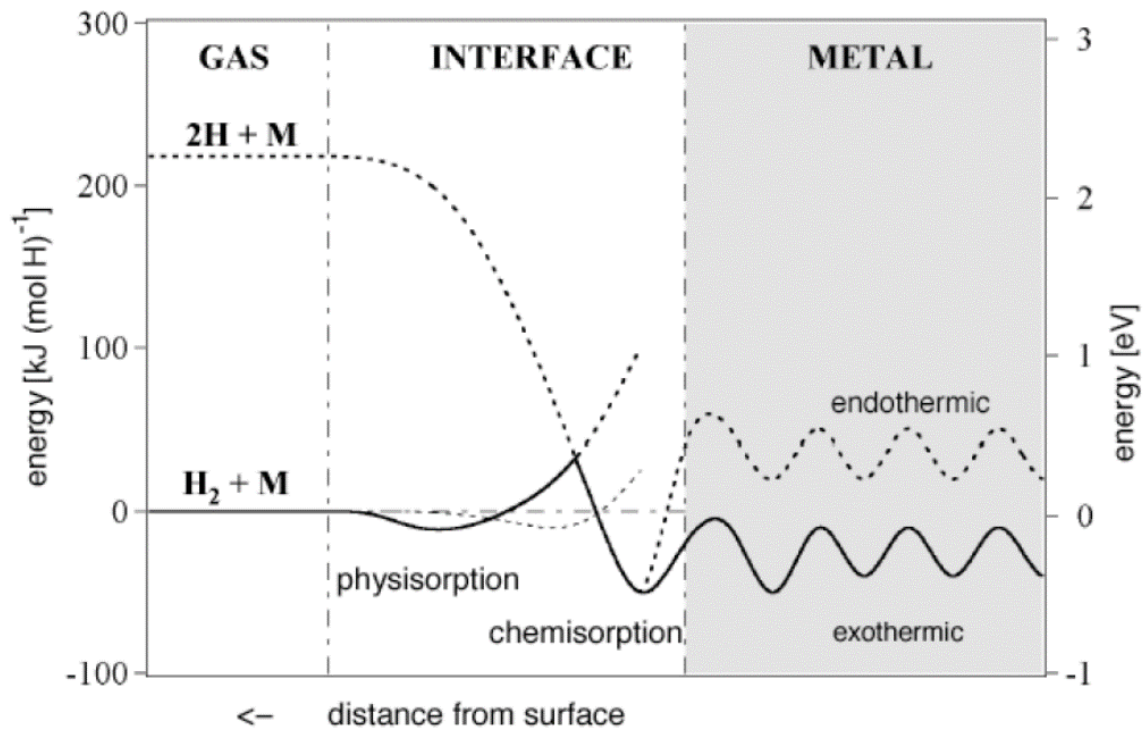
Figure 1.2: One-dimensional potential energy curve [19]
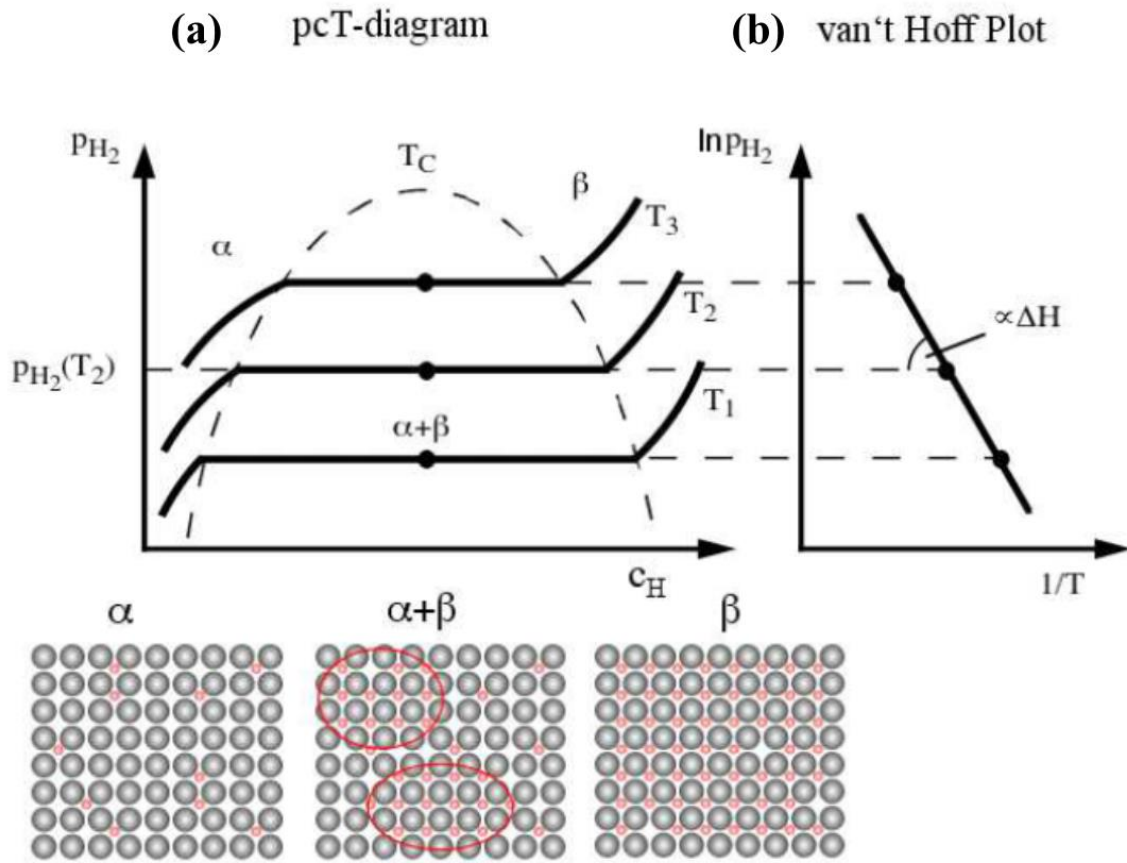
Figure 1.3: (a) Pressure Composition Isotherms (PCI) measurement & (b) van't Hoff plot [19]
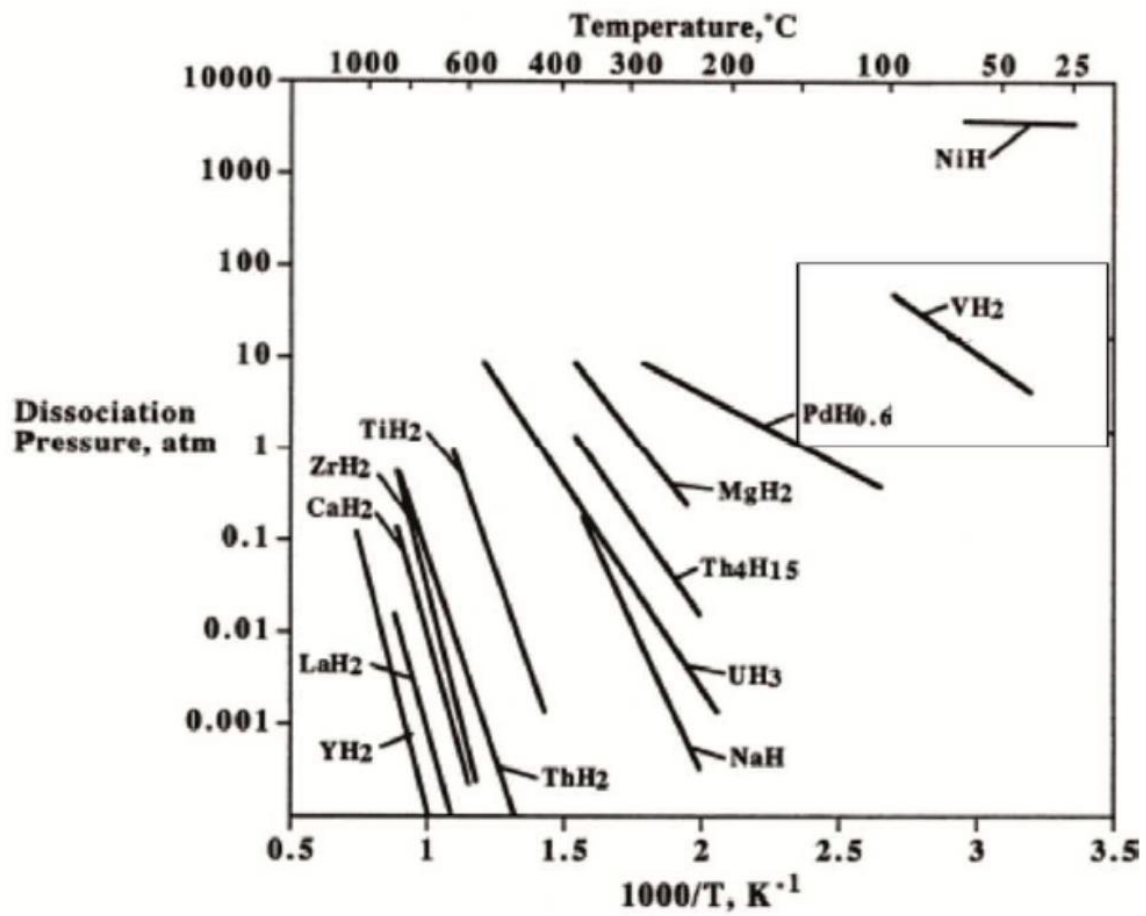
Figure 1.4: van't Hoff plots of some selected hydrides [19]
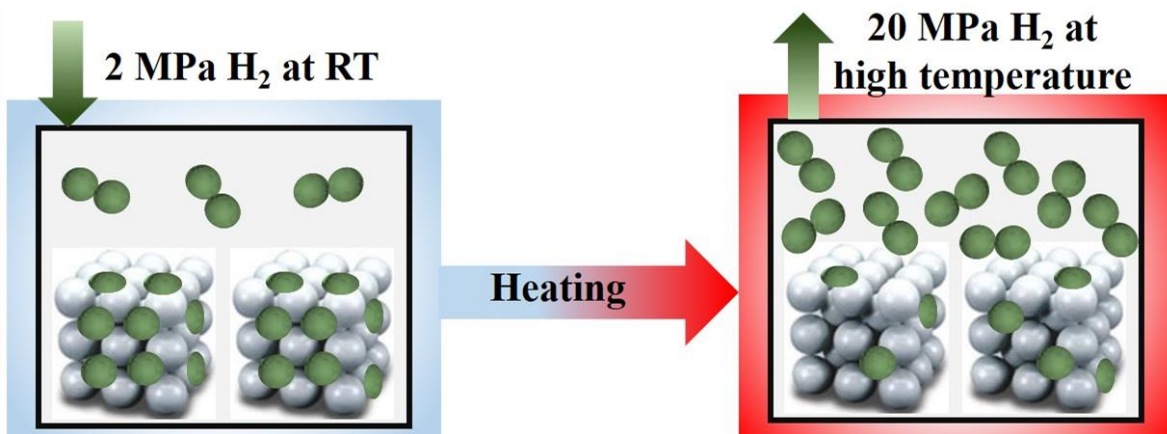
Figure 1.5: Schematic of hydrogen compression

2. Purpose of Thesis

Recently, the development of metal hydride compressor is a promising technology for hydrogen compression which has the capability of compressing hydrogen to a high pressure by the alteration of heat only without any moving parts thus considered no mechanical fatigue. In order to realize metal hydride based compressor, the material should possess favorable sorption properties as well as cyclic durability at high temperature and pressure conditions. This forms the purpose of my thesis. In this work, V-Ti-Cr BCC (body-centered cubic) alloys were chosen due to their favorable PCT window and suitable cyclic durability at moderate conditions. In connection, the studied materials are a low vanadium containing alloy $V_{20}Ti_{32}Cr_{48}$, and a high vanadium containing alloy $V_{40}Ti_{21.5}Cr_{38.5}$. A systematic study of their sorption properties, as well as structural and morphological properties, are being presented in this thesis. In the second part of this thesis, an effort has been carried out to improve the cyclic performance of high vanadium containing $V_{40}Ti_{21.5}Cr_{38.5}$ alloy further. The fourth element has been substituted for Cr. According to previous studies at room temperature, Nb, Fe, and Zr were found effective to enhance the cyclic stability of V-Ti-Cr alloys, the above elements were selected to observe their

effect at high temperature and pressure conditions. All the above alloys were tested for their sorption properties using PCT curves at a different temperature. The compressor test was performed in the range of 0.07 MPa – 20 MPa with the temperature range of RT – 310°C. The effect of such hard conditions on their sorption performance has been evaluated in terms of their structural changes and the detailed mechanism has been proposed herein.

3. Experimental procedures

3.1 Sample preparation

All the V-Ti-Cr based BCC alloys were purchased from Japan metals and chemicals Co Ltd., which is prepared by arc melting of starting materials (purity > 99.9%) in the respective molar ratio. The samples were melted three times under argon atmosphere to ensure homogeneity. To improve the crystallinity and to dissolve some minor phases, the samples were annealed at 1500K for 24h.

Table 3.1 Materials for this work

Parent materials	$V_{40}Ti_{21.5}Cr_{38.5}$			$V_{20}Ti_{32}Cr_{48}$
Doped materials	$V_{40}Ti_{21.5}Cr_{33.5}Nb_5$	$V_{40}Ti_{21.5}Cr_{33.5}Fe_5$	$V_{40}Ti_{21.5}Cr_{33.5}Zr_5$	-

3.2 Experimental Technique

3.2.1 Powder X-ray diffraction (XRD) and synchrotron radiation XRD (SR-XRD)

Principle

Powder X-ray diffraction is the method to identify the crystal structure, to determine the lattice parameters and the phases of materials. Since the crystal structures contain planes of atoms, the incident X-ray beam interacts with atoms in crystals and get reflected from each plane to produce interference thus forming the diffraction pattern. The distance between the lattice plane 1 and 2 is d_{hkl}, where *hkl* are Miller indexes as shown in Fig 3.1. Ray-a reflects off from the top atomic plane while Ray-b reflects from the second atomic plane. The constructive interference occurs when two reflected beams exit the crystal satisfying the following equation,

$$n\lambda = 2d_{hkl} \sin\theta \qquad (3.1)$$

This diffraction condition is known as Bragg's law. The diffraction angle 2θ is between the incident X-ray (S_0) and diffracted X-ray (S_1) as shown in Fig 3.1. XRD pattern obtained from the different lattice planes [54].

The Debye Scherrer equation for calculating the crystallite size is written as:

$$D = \frac{K\lambda}{\beta cos\theta}$$ (3.2)

Where K is the Scherrer constant, λ is the wavelength of light used for the diffraction, β is the "full width at half maximum" of the peaks, and θ is the angle measured. The Scherrer constant (K) in the above formula accounts for the shape of the particle and is generally taken to have the value 0.9 [55].

Synchrotron radiation XRD (SR-XRD) gives high-resolution diffraction data because the synchrotron radiation X-ray has higher directivity than the laboratory source and monochrome beam. Therefore, the peaks corresponding to the low-crystalline phase and small peaks in the profile of the crystal can be observed by SR-XRD [56].

Procedure

In this work, the phases and crystal structures of all the samples were examined by the powder XRD measurements (Rigaku, RINT-2500) as shown in Fig 3.2 (a). The X-ray source was Cu-Kα (λ=0.154nm) operated under 40 kV, 200 mA. The sample was spread on the glass plate spread with high vacuum grease (Apiezon®, M&I Material Ltd.) as a glue. All the samples were covered with a

polyimide sheet (Kapton®, Du Pont-Toray Co. Ltd) of 8 μm thickness to avoid an oxidation during the measurement and all this process was carried out inside the glove box filled with highly pure Ar as shown in Fig 3.2 (b). The SR-XRD measurements were performed by using a large Debye–Scherer camera with an imaging plate at the beamline BL5S2 General Material Evaluation I (X-ray diffraction) (Aichi Synchrotron Radiation Center). The samples used for the SR-XRD experiments were stuffed in glass capillaries with 0.01 mm in thickness, 0.50 mm in diameter and 80 mm in length (Hilgenberg), which were sealed with an epoxy adhesive. The wavelength of the X-ray beam used in this study was 1.0 Å with the photons of 12.4 keV energy as calibrated by the lattice constant of ceria CeO_2 at room temperature. The obtained XRD patterns were analyzed by using a software PDXL with powder diffraction files (PDF) as the database.

3.2.2 Scanning Electron Microscopy (SEM)

Principle

Scanning electron microscope (SEM) is the important technique for obtaining the detailed information about the surface morphology of the samples as well

as qualitative and quantitative determination of the elemental compositions of the samples using X-ray detectors coupled with it.

When an electron beam interacts with the solid specimen, it can generate a wide variety of signals which is a secondary electron, Auger electron, backscattered electron, characteristic X-ray, cathodoluminescence and scattering electron as shown in Fig 3.3. The incident electron beam is generated by an electron gun and the SEM image obtained from the surface of the sample by the emission of the secondary electrons and reflected electrons. The electron beam can easily react with gas molecules in the air. Therefore, the sample chamber is kept under a vacuum of 10^{-3} to 10^{-4} Pa pressure range to avoid the air contamination and to allow the electrons to reach the sample [57].

Procedure

In this study, SEM (JEOL, JIB-4600F/HKD) was used to observe the morphology of the samples, as shown in Fig 3.4 (d). The sample was spread on the carbon tape in the sample holder inside the glove box. Then the samples were covered with a polyimide sheet (Kapton®, Du Pont-Toray Co. Ltd) of 8 μm thickness to avoid an oxidation during the transfer of samples to SEM chamber. The samples were transferred to the SEM chamber without exposure

of the sample to the air using a specially designed arrangement as shown in Figs 3.4 (a)-(c). The acceleration voltage was fixed at 10kV.

3.2.3 Energy Dispersive X-ray Spectroscopy (EDS)

Principle

Energy dispersive X-ray spectroscopy is a qualitative and quantitative X-ray microanalytical technique that provides the information of the elemental composition of the sample which are elemental mapping, point, and line analysis. The EDS spectrum is obtained by the emission of the characteristic X-rays from the sample.

When an incident electron beam collides with the atom of the sample, an inner shell electron ejected from the atom. Then the higher energy level electron transfer into the lower energy level to fill the vacancy which is occurred by emitting characteristic X-ray as shown in Fig 3.5. The characteristic X-ray depends on the elements, therefore the EDS is used to find the elements and the composition of the material by the intensity of each characteristic X-ray.

Procedure

The composition of the alloy material was estimated by EDS equipped with SEM (JEOL, JIB-4600F/HKD) experiment as shown in Fig 3.4 (d). The

measurements were performed on the same samples used for SEM at the same time. In this work, the estimation of the atomic ratio carried out at the several points on the samples.

3.2.4 Transmission Electron Microscopy (TEM)

Principle

Transmission electron microscope (TEM) is an important technique to obtain the detail information about the crystal structure, microstructure and chemical composition of the samples in the micrometer or nanometer range. An incident accelerated high voltage electron beam pass through an electromagnetic condensing lens and the thin beam of electrons interacts with the ultra-thin material that can generate different signals. Some electrons elastically scattered without losing the energy, some electrons inelastically scattered with the partial energy loss, some electrons penetrate the material without any interaction and pass through the intermediate lenses as shown in Fig 3.6. These transmission electrons give an image of the sample.

Procedure

In this study, the microstructure of the samples was investigated by TEM (JEOL, JEM-2010) using plastic bag method [61]. The samples were spread on the Mo

grid in the TEM sample holder placed inside the glove box. Then the TEM sample holder was kept in the main area of the plastic bag filled with high purity of Ar gas thus allowing the sample transfer to the TEM apparatus without any oxidation. After that, the plastic bag was connected with TEM by using a binding tape and the air from the joining section was replaced with continuous flushing Ar gas for few minutes.

3.2.5 Pressure-Composition Isotherm (PCI)

Principle

Pressure-composition isotherm (PCI) is the technique to understand the hydrogen sorption behavior of metal hydride materials and alloys by the isothermal measurement of the equilibrium gas concentration pressure-composition-temperature (PCT) data which is the function of the surrounding gas pressure in materials [62, 63]. Generally, isothermal measurements are used as an evaluation technique of hydrogen storage alloys. There are two methods for the measurements of hydrogen absorption and desorption isotherms which are sieverts volumetric and gravimetric methods. Sievert's type volumetric method can estimate composition by measuring the change in pressure of samples according to their known system volume. A gravimetric method can

evaluate composition by measuring the change in weight of samples. The sieverts type apparatus consists of a gas reservoir and sample holder which are separated by a valve with the known volume V_R and V_S, respectively as shown in Fig 3.7 (a). To achieve an isothermal condition by heating the sample holder, only "reactor" part is heated to high temperature and remaining "line" part is at room temperature. The reactor and line volume was measured by blank PCI measurement (without sample). The determination of composition measurement, the temperature is held constant at $T_R = T_L = T_l$ (low temperature) and $T_a = T_h$ (high temperature). The gas density $d(p, T)$, moles of gas per volume, is evaluated from measured pressure and temperature using an appropriate equation of state, and a mole of gas n derives as $d(p, T)V$, where, volume V, temperature T, and pressure p with their subscript R, L, and 'a' denote the reservoir, line, and reactor, respectively.

At the initial state, moles of gas can be expressed as

$$n = d(p_R, T_l)\ V_R + d(p_L, T_l)\ V_L + d(p_a, T_h)\ V_a$$

where $p_L = p_a \neq p_R$ with the valve closed ($p_a < p_R$ for absorption by introducing the gas to the reservoir, $p_a > p_R$ for desorption by evacuating the reservoir).

After opening the valve, the pressure change is monitored until the system reaches an equilibrium state with moles of gas n':

$$n' = d(p_R', T_l) V_R + d(p_L', T_l) V_L + d(p_a', T_h) V_a$$

where $p_R' = p_L' = p_a' = p'$. This difference between n and n' gives the amount of gas absorbed or desorbed in solid samples. As a result, one set of pressure and composition data is derived, and the measurement is continiued by increasing or decreasing the pressure.

Procedure

Hydrogen sorbing properties of this study were investigated by Sieverts-type apparatus (Suzuki Shokan Co.Ltd.) as shown in Fig 3.7 (b). The sample (1g and 13g) was taken into the sample holder and the activation process was performed before real PCI measurements/compressor tests which is important to remove the surface contaminations and produce a fresh surface for hydrogen exposure. For the activation, the alloy powder was exposed to 5MPa hydrogen at room temperature (RT) which was increased up to 100°C and keep it for 4hrs at this temperature, then the sample holder was evacuated and keep it for 2 hrs at the same condition. This whole process was repeated 3 times to activate the sample completely. Finally, the sample was kept at 200 ºC for 6 hrs under a dynamic

vacuum to ensure complete hydrogen desorption. After the activation, the pressure-composition Isotherms were measured in the range of temperature 22°C - 100°C and the pressure range 0.001 MPa - 6 MPa. The reservoir volume V_R was measured as 25.978 cm³, while the line volume V_l and the reactor volume V_a were measured as 10 cm³ and 20.6 cm³, respectively.

3.2.6 Compressor cycling system

Compressor cycling system is the important homemade technique to evaluate the compressor cyclic performance of alloy materials for practical applications [64]. Basically, low-pressure hydrogen gas is absorbed at an ambient temperature and high-pressure hydrogen gas can be obtained at high temperature for metal hydride based hydrogen compressor. The schematic diagram of the compressor system for this study is shown in Fig 3.8. The compressor cyclic tests were performed in a closed sample holder by achieving 20 MPa in temperature range RT - 310 °C with 13g sample into the sample holder. Low-pressure hydrogen gas was exposed to material in the sample holder at RT. Then after complete absorption of hydrogen gas at RT, the sample holder was closed and the temperature was increased (heating rate 5° C/mins) by the furnace to reach the target pressure. After that, the sample holder was

cooled down to RT in order to decrease the pressure to initial value. The whole process was considered as 1 cycle. The compressor cyclic tests as described above were performed up to 100 cycles. Finally after all the cycling hydrogen completely desorbed under vacuum condition with high temperature.

Figures
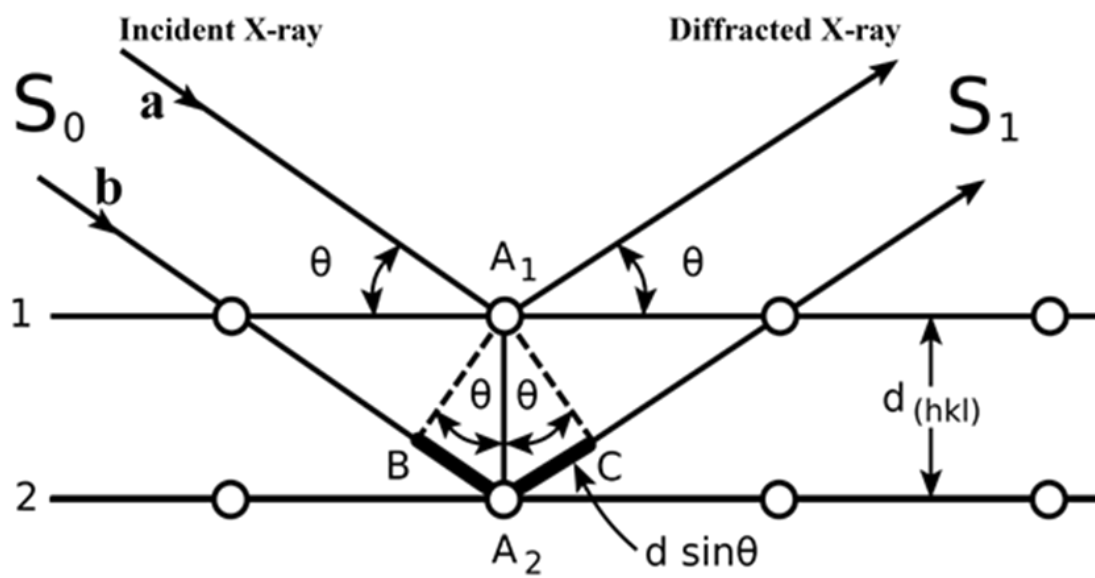
Figure 3.1: Diffraction of X-ray from lattice planes in the crystal [56]
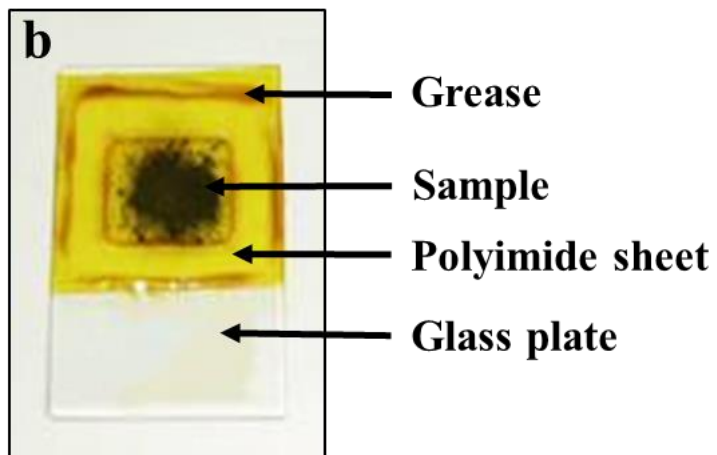
Figure 3.2: (a) XRD equipment, (b) Sample preparation
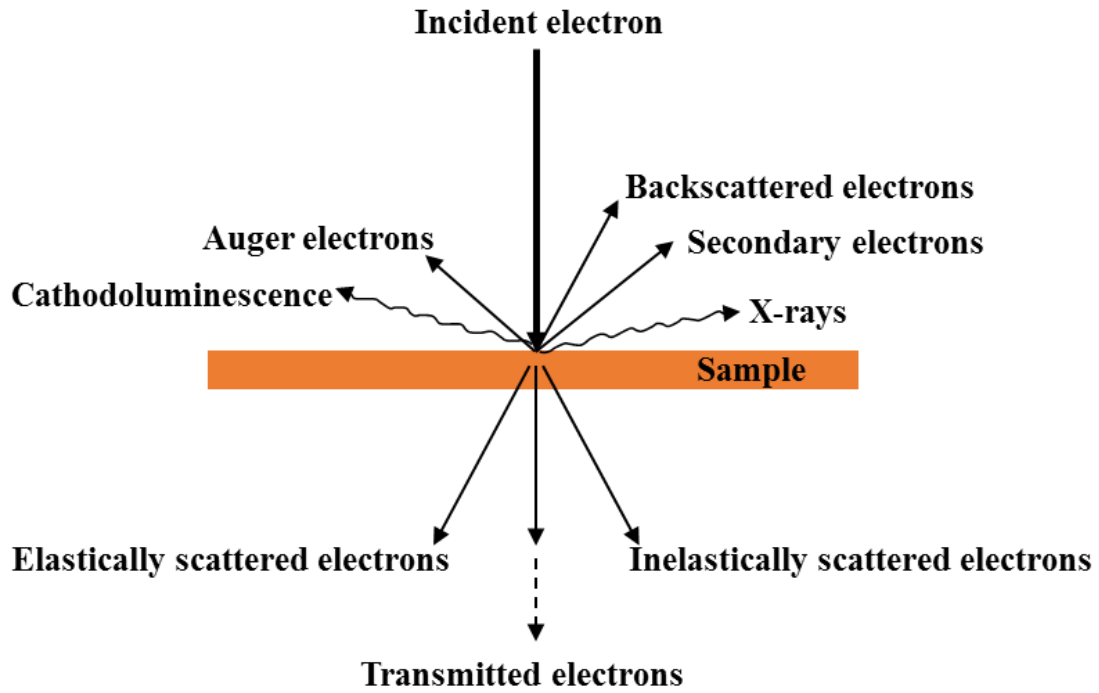
Figure 3.3: Interaction between the incident electron and material
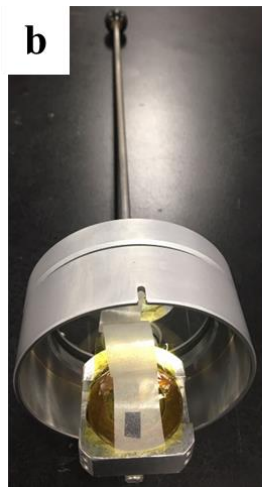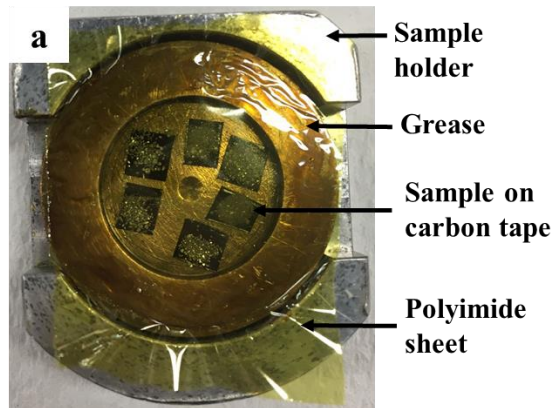
Figure 3.4: (a) Sample preparation, (b) & (c) Sample transferring to SEM chamber, (d) SEM equipment
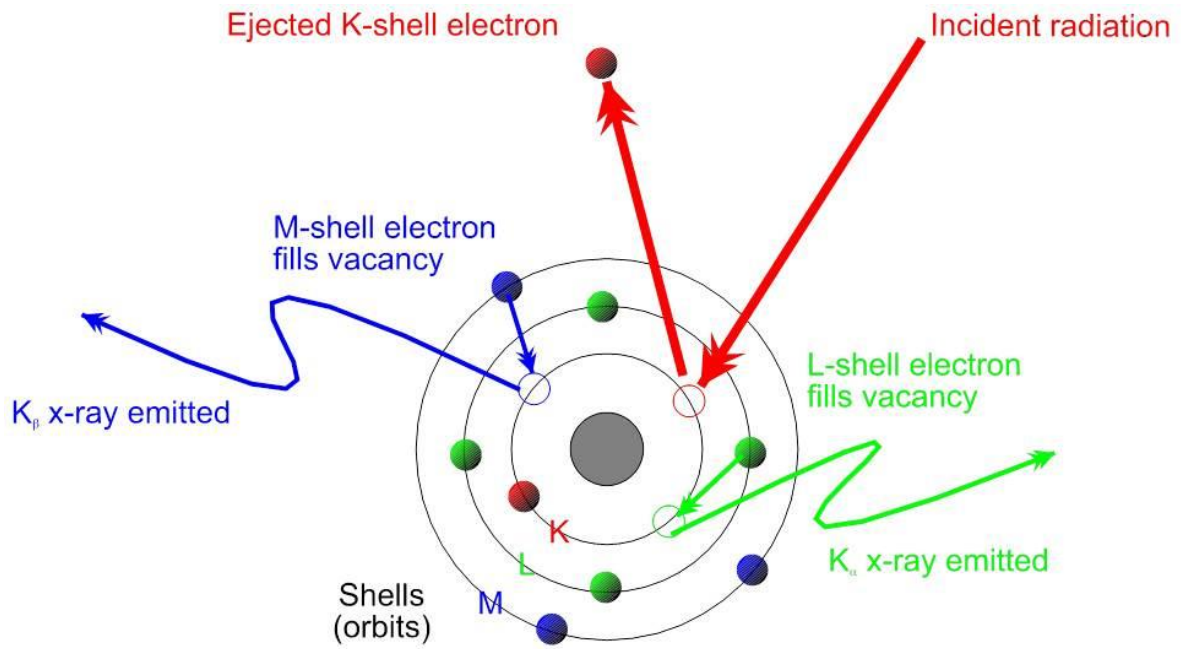
Figure 3.5: Characteristic X-ray generation [59]
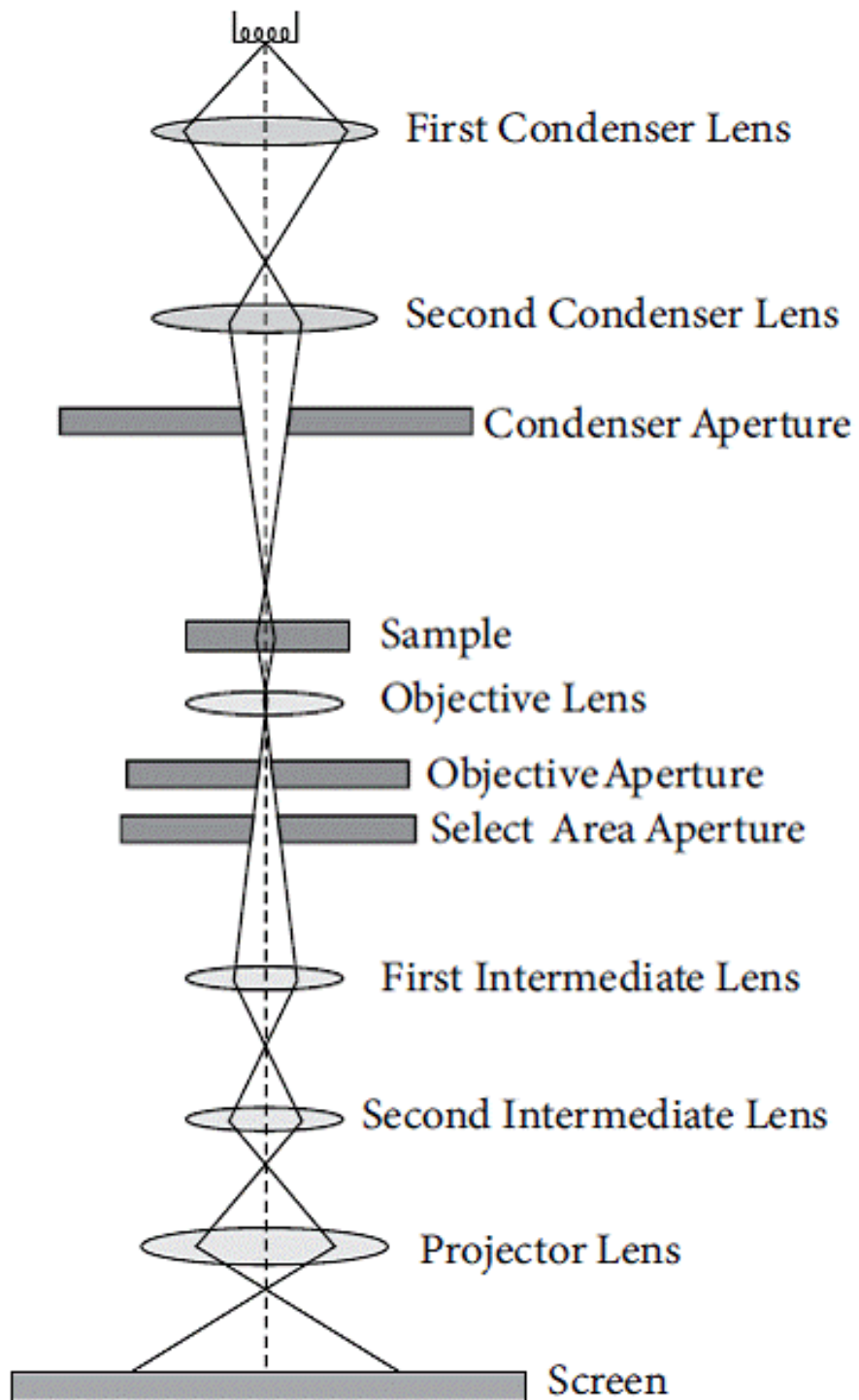
Figure 3.6: Working principle of TEM [60]

a

Reservoir p_R, V_R, T_R

Pressure Gauge (MPa)

gas cylinder

Sample holder

Line p_L, V_L, T_L

Reactor p_a, V_a, T_a

Vacuum pump

$V_S = V_L + V_a$

b
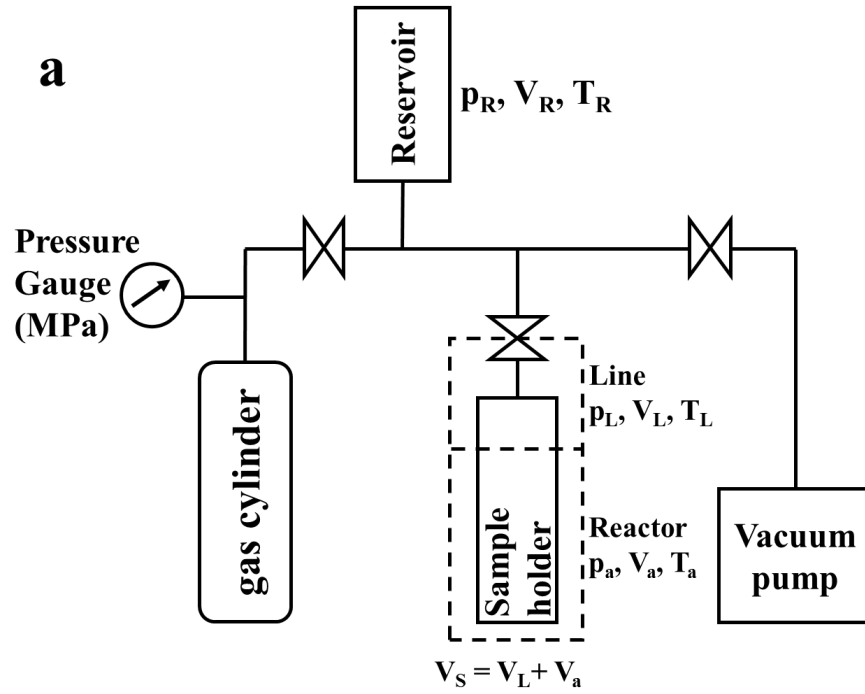
Figure 3.7: (a) Schematic of Sievert's type measurement, (b)PCI equipment
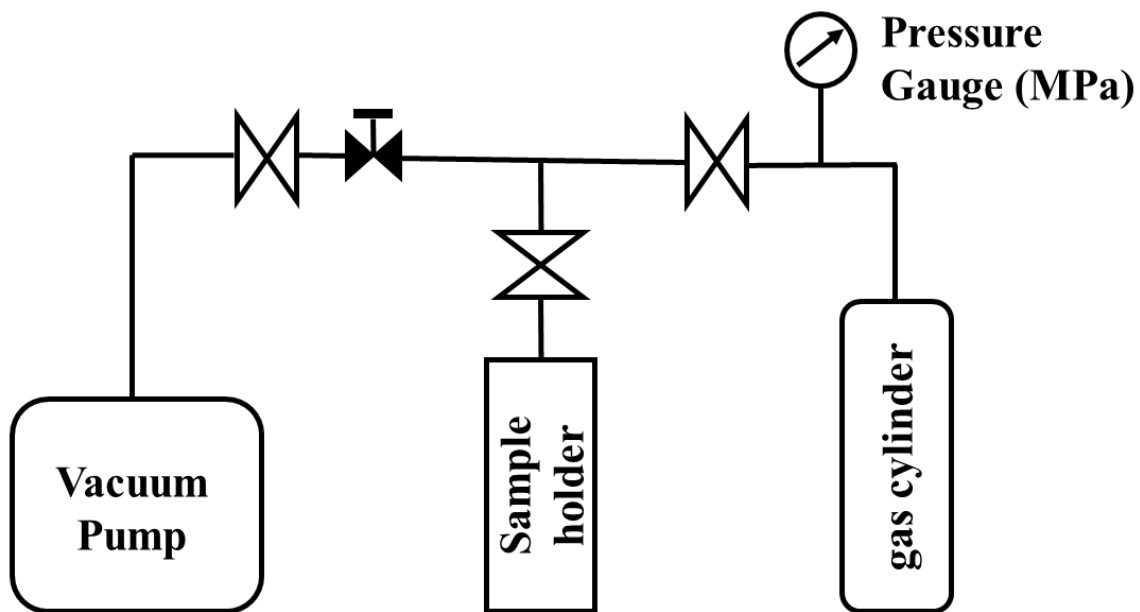
Figure 3.8: Schematic of the compressor system

4. Results and Discussion

4.1. Sorption properties of V-Ti-Cr BCC alloys

This section describes the properties of two BCC alloys as parent material i.e. high vanadium containing $V_{40}Ti_{21.5}Cr_{38.5}$ and low vanadium containing $V_{20}Ti_{32}Cr_{48}$ alloys in terms of their structural, morphological and hydrogenation characterization.

4.1.1. Structural and morphological characterization

The XRD profile for both pristine samples of $V_{40}Ti_{21.5}Cr_{38.5}$ and $V_{20}Ti_{32}Cr_{48}$ alloys could be indexed by the BCC structure of vanadium as shown in Fig 4.1. The peaks are shifted to the lower angle side for both alloys after 100 cycles of compressor test, which shows the lattice expansion in the unit cell of the samples. This is supposed to be associated with a small amount of hydrogen left in the samples; even after the samples were heated at 200°C after cyclic compressor test. In addition, the peaks are broadened after cycling that can be suggested due to crystallite size refinement during hydrogen absorption/desorption cycles. The crystallite size of $V_{40}Ti_{21.5}Cr_{38.5}$ and $V_{20}Ti_{32}Cr_{48}$ alloys has been found to be reduced from 26.8 and 24.4 nm for pristine to 21.6 and 15.5 nm for cycled samples, which is calculated by using

Debye Scherrer equation ($D = K\lambda/\beta\cos\theta$). Besides, multiple peaks can be seen in the XRD profile of cycled $V_{20}Ti_{32}Cr_{48}$ alloy, particularly at around 36° and 40°, which could be indexed by $TiH_{0.66}$ and $VH_{0.81}$ phases that occurs because of the phase separation and disproportionation of the original alloy during sorption cycling. The crystal structure of $TiH_{0.66}$ and $VH_{0.81}$ phases is orthorhombic and tetragonal respectively.

Fig 4.2 shows the morphology of both V-Ti-Cr alloys. The SEM images of pristine and cycled $V_{40}Ti_{21.5}Cr_{38.5}$ samples are shown in Fig 4.2 (a), (b), whereas Fig 4.2(c), (d) shows the SEM images of pristine and cycled $V_{20}Ti_{32}Cr_{48}$ samples. These images show the particle size reduction during sorption compressor cycling for both alloys. The particle size of pristine samples for both alloys is found in the range of 5-100 μm which is reduced down 1-50μm during compressor cycling for both alloys.

To confirm the microstructural phase segregation the higher magnification EDS was performed and the atomic percentage of elements at a different position for both pristine and cycled alloys are shown in the table with Fig 4.3. The tables in Fig 4.3 (a), (c) show the elemental ratio of both pristine samples very close to the targeted compounds throughout the samples which suggest that the alloys

are homogeneous at microstructure level. The homogeneity remains same for $V_{40}Ti_{21.5}Cr_{38.5}$ alloy even after 100 cycles as shown in Fig 4.3 (b). In contrast, $V_{20}Ti_{32}Cr_{48}$ alloy has been found disproportionate after cycling as shown in Fig 4.3 (d). The EDS analysis at point 1 and point 2 suggest that the original material has been segregated in Ti-rich phase, while at point 4 V-rich phase has been observed. It is in line with the XRD results where the TiH_2 phase is observed for the cycled $V_{20}Ti_{21.5}Cr_{38.5}$ sample.

TEM measurements have been performed to identify the exact phases at Nano-scale for pristine and cycled sample of both alloys and the results are shown in Fig 4.4 and 4.5. A small area from the bright field image of the sample edge is selected and the selected area diffraction patterns were analyzed as shown in Fig 4.4a. The diffraction patterns are characterized by the (110), (1-10), and (200) planes of $V_{40}Ti_{21.5}Cr_{38.5}$ phase as shown in the right image. Fig 4.4 (b) shows the bright, dark field images and the Cr diffraction spot was used for the corresponding SAED pattern of the same alloy after 100 cycles. The same structure as that of the pristine sample can be observed from the diffraction patterns as a major phase. In addition, very weak diffraction spots are also present which implies that a small amount of Cr is segregated from the $V_{40}Ti_{21.5}Cr_{38.5}$ after 100 cycles.

Fig 4.5 shows the TEM results for pristine and cycled $V_{20}Ti_{32}Cr_{48}$ alloys. The single crystal of pristine alloy is observed from the diffraction patterns, which is characterized by the (110), (101), and (211) planes from the sample as shown in Fig 4.5 (a). The bright field, dark field images and selected area electron diffraction (SAED) patterns for cycled $V_{20}Ti_{32}Cr_{48}$ alloy is shown in Fig 4.5 (b)-(e). Fig 4.5 (b) shows the diffraction patterns corresponding to the main phase similar to the original sample. However, the different phases are also found, which are identified as $VH_{0.81}$ (Fig 4.5c) and $TiH_{0.66}$ (Fig 4.5d and e) by analyzing the corresponding single crystal diffraction patterns. This result is in good agreement with XRD and SEM/EDS results.

4.1.2. Hydrogen storage properties of V–Ti–Cr alloys

PCI curves at RT (room temperature) for both $V_{40}Ti_{21.5}Cr_{38.5}$ and $V_{20}Ti_{32}Cr_{48}$ alloys are shown in Fig 4.6 which were performed after 10, 25, 50, 100 cycles of compressor test. The maximum hydrogen capacity of the $V_{40}Ti_{21.5}Cr_{38.5}$ alloy is decreased from 2.35wt% to 1.88 wt%, with absorption and desorption plateau shifted to 0.85 MPa and 0.25 MPa during the first 10 cycles. After 10 cycles, the PCI curves are found to be quite similar up to 100 cycles which confirms the cyclic stability of this alloy as shown in Fig 4.6 (a). In contrast, the hydrogen content of $V_{20}Ti_{32}Cr_{48}$ alloy continues decreasing and reach 1.26 wt% from 2.36

wt% after 100 cycles which confirms the material degradation as shown in Fig 4.6 (b).

Fig 4.7 (a) and (b) shows the PCT curves for both pristine alloys at RT, 50°C, and 75°C. The hydrogen absorption capacities are found to be 2.44 wt% and 2.90 wt% for $V_{40}Ti_{21.5}Cr_{38.5}$ and $V_{20}Ti_{32}Cr_{48}$ alloys respectively. Here it is interesting to note that the capacity in Fig. 4.6 and 4.7 are slightly different, which must be associated with the different amount of sample i.e. 13 g (Fig. 4.6) and 1 g (Fig. 4.7). The 13g sample is tightly packed in the sample holder, so provide less surface area to hydrogen or allow slow diffusion of hydrogen through the sample, thus lower the hydrogen capacity in comparison to 1g sample, which is completely exposed to hydrogen very easily. The absorption and desorption plateau pressures at RT are found to be 1.5 MPa and 0.25 MPa is for $V_{40}Ti_{21.5}Cr_{38.5}$ alloy while 0.9 MPa and 0.06 MPa for $V_{20}Ti_{32}Cr_{48}$ alloy, respectively. In addition, the hysteresis is larger for the $V_{20}Ti_{32}Cr_{48}$ alloy as compared to the $V_{40}Ti_{21.5}Cr_{38.5}$ alloy. The thermodynamic parameters of enthalpy (ΔH) and entropy (ΔS) values are obtained using Van't Hoff plot as shown in Fig 4.7 (c). The enthalpy values for $V_{40}Ti_{21.5}Cr_{38.5}$ and $V_{20}Ti_{32}Cr_{48}$ alloys are found to be -41 and -39 kJ mol^{-1}H$_2$, respectively, these values are very close to VH$_2$ [65]. The higher enthalpy value indicates the lower dissociation

pressure, higher stability of the hydride and higher dehydrogenation temperature. The entropy value for $V_{40}Ti_{21.5}Cr_{38.5}$ and $V_{20}Ti_{32}Cr_{48}$ alloys are calculated as 146 J mol^{-1} H$_2$ and 128 J mol^{-1} H$_2$. The higher entropy value of $V_{40}Ti_{21.5}Cr_{38.5}$ in compare to $V_{20}Ti_{32}Cr_{48}$ alloy suggests a higher disorder of H$_2$ in the host lattice of $V_{40}Ti_{21.5}Cr_{38.5}$.

Fig 4.8 shows the PCT curves for both $V_{40}Ti_{21.5}Cr_{38.5}$ and $V_{20}Ti_{32}Cr_{48}$ alloys after 100 cycles of compressor test. The high vanadium content alloy i.e. $V_{40}Ti_{21.5}Cr_{38.5}$ has quite stable curves as shown in Fig 4.8 (a) with a clear plateau region. The plateau pressure is found to be increased with an increase in temperature which is a characteristic feature of the PCT curve. In contrast, $V_{20}Ti_{32}Cr_{48}$ alloy (Fig 4.8 b) shows no clear plateau. Surprisingly, the capacity is found to be increased with increasing temperature and no solid solution region appeared which is because of already remained hydrogen in the material. It can be explained on the basis of some kinetically inactive phase formation during cycling, which cannot absorb hydrogen at room temperature, but only at higher temperature, thus enhancing the sorption capacity with increasing the temperature. This result is supported by XRD (Fig 4.1) and TEM (Fig 4.5) results which suggest the segregation of $TiH_{0.66}$ and $VH_{0.81}$ phases after cycling

of the $V_{20}Ti_{32}Cr_{48}$ alloy and disproportionate the composition of the parent alloy thus forming kinetically inactive phase at room temperature.

4.1.3. Compressor cyclic test

4.1.3.1 Pressure based compressor test

Since these BCC alloys were employed to develop double stage hydrogen compressor to achieve 80 MPa [66], their compressor cyclic test at high pressure and temperature is quite important. The compressor cyclic performance for both $V_{40}Ti_{21.5}Cr_{38.5}$ and $V_{20}Ti_{32}Cr_{48}$ alloys to achieve 20 MPa pressure is shown in Fig 4.9 (a) and (b). To record these profiles, the initial pressure at room temperature (~22°C) was kept at 0.07 MPa and 2 MPa for $V_{20}Ti_{32}Cr_{48}$ and $V_{40}Ti_{21.5}Cr_{38.5}$ alloys, respectively according to their desorption plateau pressures. At first, the samples were charged at 5 MPa H_2 gas to achieve their complete storage capacity and then the selected initial pressure was maintained by removing excess H_2 gas from the chamber. The target pressure for the first stage compressor was decided as 20 MPa [66, 67]. To achieve this high pressure, the sample holder was heated up to 160°C and 310°C for $V_{40}Ti_{21.5}Cr_{38.5}$ and $V_{20}Ti_{32}Cr_{48}$ alloys respectively. After that, the sample holder was cooled down to RT in order to reduce the pressure to an initial value, the whole process was

considered as 1 cycle. The compressor cyclic test as described above was performed up to 100 cycles. To make it clear for the readers, the data for only 10 cycles are shown in Fig 4.9 (a) and (b). The plateau pressure of the $V_{40}Ti_{21.5}Cr_{38.5}$ and $V_{20}Ti_{32}Cr_{48}$ alloys at 160°C and 310°C are calculated by using experimentally determined ΔH and ΔS values (Eqn 1.14), which are found to be 48 MPa and 155 MPa for $V_{40}Ti_{21.5}Cr_{38.5}$ and $V_{20}Ti_{32}Cr_{48}$ alloys, respectively.

Hydrogen pressure in the sample holder at room temperature was measured for the cyclic stability of the alloys as shown in Fig 4.10. The pressure increase inside the sample holder at room temperature after each cycle is a direct measure of remained excess gaseous hydrogen, which could not be absorbed by the material. The remaining gaseous hydrogen can be used to estimate the degradation of the material. It is clearly observed that the pressure in the sample holder containing $V_{40}Ti_{21.5}Cr_{38.5}$ alloy is increased from 2 MPa to 4 MPa at RT in the first 10 cycles and then remain stable up to 100 cycles. Whereas, the pressure in the sample holder with $V_{20}Ti_{32}Cr_{48}$ alloy, continuously increase up to 100 cycles. This shows that the material having less vanadium content alloy is continuously degrading, whereas high vanadium content alloy is quite stable after 10 cycles. The initial storage capacity decay for $V_{40}Ti_{21.5}Cr_{38.5}$ alloy must

be due to the remaining hydrogen in solid solution and/or stable β-phase hydride, this is in line with XRD result (Fig 4.1 a) where a peak shift to lower angle has been observed for cycled $V_{40}Ti_{21.5}Cr_{38.5}$ alloy, that suggests residual hydrogen which could not be desorbed at the studied temperature range and remained in the alloy as dead hydrogen. However, a continued degradation of the $V_{20}Ti_{32}Cr_{48}$ alloy is associated with the gradual formation of $TiH_{0.66}$ and $VH_{0.81}$ with no. of cycles as observed from XRD, SEM/EDX, and TEM results.

4.1.3.2 Temperature based compressor test

In the previous section, the temperature was varied to achieve 20 MPa pressure, however, the temperature was hugely different for both alloys. Thus it is necessary to differentiate the effect of temperature and pressure on the sorption properties and to see the effect of both the alloys. This section comprises the results of compressor cyclic test by keeping the maximum temperature fixed at $200^{\circ}C$. The compressor cyclic test was performed up to 20 cycles with the initial pressure as 2 MPa and 0.07 MPa for $V_{40}Ti_{21.5}Cr_{38.5}$ and $V_{20}Ti_{32}Cr_{48}$ alloy at RT respectively. As observed in Fig 4.11 (a) and (b), the pressure could reach up to 20 MPa and 12 MPa for $V_{40}Ti_{21.5}Cr_{38.5}$ and $V_{20}Ti_{32}Cr_{48}$ alloys at 200 $^{\circ}C$ respectively. The variation in H_2 pressure with no. of cycles in the sample holder

at room temperature and at 200 °C for both alloys is shown in Fig 4.11 (c) and (d). It is quite interesting to note that the pressure at room temperature in the sample holder containing $V_{40}Ti_{21.5}Cr_{38.5}$ alloy became stable after 1 cycle in contrast to 10 cycles needed during pressure-based compressor test (Fig. 4.10). This suggests that a stable phase could be formed immediately at 200°C that is much faster than 160°C, needed for the pressure based compressor cyclic test (Fig. 4.9a). Similarly, the heating of the sample holder up to 200°C containing $V_{20}Ti_{32}Cr_{48}$ alloy could reach only up to 12 MPa H_2 (Fig 4.11 (d)). The pressure at room temperature is found much stable in comparison to that observed for the compressor test performed with 20 MPa and 310°C (Fig. 4.9b). The modest pressure and temperature conditions allow this alloy to keep its stability much better. Fig 4.11 (e) and (f) shows the PCI curves at RT for both alloys before and after 10 compressor cycles. The hydrogen capacity for both $V_{40}Ti_{21.5}Cr_{38.5}$ and $V_{20}Ti_{32}Cr_{48}$ alloys is found to be 1.93 wt% and 2.16 wt% after 10 compressor cycle test which is slightly higher than 1.86 wt% and 2.03 wt% for corresponding alloys after 10 compressor cycle tests with higher pressure/temperature conditions (Fig 4.6).

Considering the pressure and temperature based compressor cyclic test, high vanadium content $V_{40}Ti_{21.5}Cr_{38.5}$ alloy requires only 160°C to achieve 20 MPa

hydrogen pressure due to higher value of plateau pressure while low vanadium content $V_{20}Ti_{32}Cr_{48}$ alloy requires 310°C to achieve 20 MPa hydrogen pressure due to the low plateau pressure. The high V containing alloy get stable after 10 cycles of pressure based compressor test, whereas it get stable immediately after 1 cycle during the temperature based compressor test because of high temperature, which accelerate the formation of stable phase. On the other hand, low vanadium content alloy shows different behaviour when heated to 200 °C in comparison to 310°C, required to achieve 20 MPa pressure during pressure based compressor test. It shows very stable performance over no. of cycles because it could reach only 12 MPa at this temperature, thus undergone through very mild conditions. So it is clear that the less temperature and suitable plateau pressure are the important factors to achieve 20 MPa pressure with nice stability.

4.2   The effect of the fourth element on the cyclic performance of the $V_{40}Ti_{21.5}Cr_{38.5}$ alloy

Since $V_{40}Ti_{21.5}Cr_{38.5}$ alloy has shown better performance than $V_{20}Ti_{32}Cr_{48}$ alloy in terms of its hydrogen storage capacity and cyclic stability. In order to improve the cyclic and hydrogen storage properties for $V_{40}Ti_{21.5}Cr_{38.5}$ alloy further, the fourth element has been substituted with Cr. Niobium, Iron, and Zirconium were chosen as the substituting elements due to their various merits.

Shin-ichi Towata et al. [68] studied the cyclic durability of $Ti_{25}Cr_{50}V_{25}$ alloy, they found that the Nb substitution of 5% for Cr ($Ti_{25}Cr_{45}V_{25}Nb_5$) was observed to be preferable for effective hydrogen storage capacity and cycle durability and Fe substitution the cyclic durability was improved but the effective hydrogen storage was decreased during cycling. E. Akiba, H. Iba et al [69] studied that Zr substituted AB_2 type Laves phase shows excellent catalytic effect during hydrogen absorption/desorption process. However, the properties at high temperature and pressure conditions have not been explored so far, thus this section describes the effect of these substituting elements on the cyclic stability as well as other hydrogenation properties of the $V_{40}Ti_{21.5}Cr_{38.5}$ alloy.

4.2.1 Structural and morphological observation

Fig 4.12 shows the XRD and SR-XRD profiles for all the substituted $V_{40}Ti_{21.5}Cr_{38.5}$ alloy. Since XRD peaks were quite broad and expected to have multiple peaks corresponding to different phases, it is decided to perform SR-XRD in order to get additional information due to its high energy. Unfortunately, no advantage / additional information could be obtained from the SR-XRD profile. The XRD and SR-XRD profiles for all prepared alloys except Zr substituted alloy indicated the same BCC structure as that of their parent element vanadium. In addition to main BCC phase, as prepared

60

$V_{40}Ti_{21.5}Cr_{33.5}Zr_5$ alloy shows the additional phase of $ZrCr_2$ laves phase which is crystallized in the cubic structure as shown in Fig 4.12 (e) and (f). The peaks corresponding to main V based BCC phase in XRD and SR-XRD profiles are found to be shifted to lower angle after 100 cycles of compressor test for all the alloys, which is a sign of lattice expansion due to residual hydrogen left in the samples, even if the alloys were heated at 100 °C under vacuum for 2 hrs. In addition, the peaks are broadened after cycling which must be due to crystallite refinement during sorption cycles. The behavior of substituted alloys is quite similar to the parent alloy. The Fe-substituted sample i.e. $V_{40}Ti_{21.5}Cr_{33.5}Fe_5$ alloy shows only slight peak shift in XRD and SR-XRD after cycling as shown in Fig 4.12 (c) and (d), however, for Nb substituted sample i.e. $V_{40}Ti_{21.5}Cr_{33.5}Nb_5$ shows the peak shape change especially at around 40° for XRD and SR-XRD which could be indexed by $VH_{0.81}$ phase as shown in Fig 4.12 (a) and (b). Apart from these, the XRD and SR-XRD profiles of Zr substituted sample i.e. $V_{40}Ti_{21.5}Cr_{33.5}Zr_5$ alloy suggest the existence of additional phase as observed from the peaks at around 35°, 40° for XRD and SR-XRD which could be indexed by the ZrV_2 phase. Thus the minor phase of $ZrCr_2$ laves phase in the starting sample transformed to ZrV_2 phase during the hydrogen sorption compressor cyclic test as shown in Fig 4.12 (e) and (f). Fig 4.13 shows the

morphology of all substituted V-Ti-Cr alloys. Which suggests the reduction in particle size during sorption compressor cycling for all alloys. Iron substituted sample shows the least pulverization during cycling, where the highest pulverization is observed for Zr-substituted sample.

4.2.2 Hydrogen storage properties of V-Ti-Cr-M (M=Nb, Fe, and Zr) alloys

Figs 4.14 (a), (b), and (c) show PCI curves at RT for $V_{40}Ti_{21.5}Cr_{33.5}Nb_5$, $V_{40}Ti_{21.5}Cr_{33.5}Fe_5$ and $V_{40}Ti_{21.5}Cr_{33.5}Zr_5$ alloys, respectively. The PCI experiments were performed after 10, 25, 50, and 100 cycles of compressor test. It is clearly shown that the Nb substituted $V_{40}Ti_{21.5}Cr_{33.5}Nb_5$ alloy has clear absorption and desorption flat plateau regions as compared to the other two alloys. The plateau pressure value at the middle point of plateau region is at 0.28 MPa and 0.028 MPa for absorption and desorption, respectively, which are lower than that of its parent alloy $V_{40}Ti_{21.5}Cr_{38.5}$. This is associated with the lattice expansion due to higher atomic radii of Nb (198 pm) in comparison to Cr (166 pm), thus allowing easy hydrogen accommodation in the lattice resulting in lowering the plateau pressure. In addition, the hydrogen storage capacity of the $V_{40}Ti_{21.5}Cr_{33.5}Nb_5$ alloy is found to be 2.5 wt% in the first cycle which is slightly higher than the parent alloy (2.35 wt%, Fig. 4.6a). The capacity

is found to be gradually decreased down to 2.08 wt% during 100 compressor cycle test. The same trend has been observed for Zr substituted alloy due to its larger atomic radii (206 pm) with absorption plateau at 0.209 MPa and desorption plateau at 0.016 MPa, however, the slope is slightly larger than that of Nb substituted alloy. In addition, the decay in the maximum capacity of the $V_{40}Ti_{21.5}Cr_{33.5}Zr_5$ alloy is found to be from 2.3 wt% to 1.93 wt% during the first 25 cycles. After 25 cycles the PCI curves found to be quite similar to 100 cycles which confirms the cyclic stability of this alloy. Moreover, a strange zigzag shape has been observed in the absorption PCI curves of Nb and Zr substituted alloy. This should be due to tight packing of a large amount of sample in a small volume, thus hindering the sample surface partially from the quick exposure with hydrogen. However, during the stabilizing time of pressure, some of the hydrogens could be absorbed slowly and thus reduce the pressure. It generates a pressure difference between two successive judging time when the instrument starts to record the pressure value and gives rise to zigzag shape in PCI. On the other hand, Fe substituted $V_{40}Ti_{21.5}Cr_{33.5}Fe_5$ alloy has higher plateau pressures at 3.808 MPa and 0.685 MPa for absorption and desorption, respectively. This is due to the contraction of lattice resulting from the smaller atomic radii of Fe (156 pm), thus making it difficult for hydrogen atoms to accommodate in the

lattice. The maximum H_2 storage capacity of the $V_{40}Ti_{21.5}Cr_{33.5}Fe_5$ alloy is found less i.e 1.878 wt% in comparison to its parent alloy, which further decreased to 1.00 wt% after 100 cycles. In addition to this after 50 and 100 cycles, PCI curves are found to be quite similar.

Among these three alloys, the Nb substituted $V_{40}Ti_{21.5}Cr_{33.5}Nb_5$ alloy shows better hydrogen storage capacity and the flat plateau region even after 100 cyclic compressor test. In addition, Nb substituted $V_{40}Ti_{21.5}Cr_{33.5}Nb_5$ alloy PCI curve shows better hydrogen capacity of 2.08 wt% in comparison to 1.8 wt% for parent $V_{40}Ti_{21.5}Cr_{38.5}$ alloy after 100 cycle compressor cyclic test.

Fig 4.15 shows the PCT curves for all substituted alloys at RT, 50°C, and 75°C before and after compressor cycling. The absorption and desorption plateau pressure at RT is found to be 0.21 MPa and 0.03 MPa for the pristine $V_{40}Ti_{21.5}Cr_{33.5}Nb_5$ alloy while these are slightly reduced to 0.07 MPa and 0.025 MPa for cycled $V_{40}Ti_{21.5}Cr_{33.5}Nb_5$ alloy, with a respective maximum capacity 2.63 wt% and 2.02 wt% as shown in Figs 4.15 (a) and (b). In the case of Fe substituted sample, PCI shows the maximum capacity 2.46 wt% with the absorption and desorption plateau pressure is observed at 3.68 MPa and 0.86 MPa as shown in Fig. 4.15(c). Moreover, no plateau region could be observed

at higher temperatures, i.e. 50 and 75°C, because it must be at much higher pressure than the studied range. The plateau region at RT has been shortened drastically after 100 cycles of compressor test as visible from Fig. 4.15(d). The Zr substituted pristine $V_{40}Ti_{21.5}Cr_{33.5}Zr_5$ alloy shows the absorption and desorption plateau pressure at 0.08 MPa and 0.01MPa with a maximum capacity of 2.5 wt% with the reversible capacity of 2 wt% (Fig. 4.15(e)). The plateau slope has been increased after compressor cycling, however still maintaining its maximum capacity as 1.75 wt% at RT as shown in Fig 4.15(f). The capacity in Fig. 4.15 (a), (c) and (e) are slightly different, which must be associated with the different amount of sample i.e. 13 g (Fig. 4.14) and 1 g (Fig. 4.15). The 13g sample is tightly packed in the sample holder, so provide less surface area to hydrogen or allow slow diffusion of hydrogen through the sample, thus lower the hydrogen capacity in comparison to 1g sample, which is completely exposed to hydrogen very easily.

Considering all the above results, it can be summarized that Nb substituted $V_{40}Ti_{21.5}Cr_{33.5}Nb_5$ alloy shows the better performance in comparison to other two alloys which has a flat plateau with suitable hydrogen absorption and desorption capacity even at a higher temperature. In addition, Nb substituted

alloy keeps its plateau shape even after 100 cycled sample in contrast to other two alloys where the plateau shape completely vanishes.

4.2.3 Pressure based compressor cyclic test

Fig 4.16 (a), (b), and (c) shows the compressor cyclic test for $V_{40}Ti_{21.5}Cr_{33.5}Nb_5$, $V_{40}Ti_{21.5}Cr_{33.5}Fe_5$, and $V_{40}Ti_{21.5}Cr_{33.5}Zr_5$ alloy, respectively. In order to perform compressor cyclic test, the initial pressure at RT was kept at 2 MPa as same as parent $V_{40}Ti_{21.5}Cr_{38.5}$ alloy. To start with this pressure, first the alloy was completely saturated with 5 MPa H_2 and then the excess pressure was removed from the chamber. The target pressure for compressor test was decided as 20 MPa similar to that for parent alloy. To achieve it the sample holder was needed to heat up to 217 °C for Nb substituted $V_{40}Ti_{21.5}Cr_{33.5}Nb_5$ alloy, 290 °C for Fe substituted $V_{40}Ti_{21.5}Cr_{33.5}Fe_5$ alloy and 255 °C for $V_{40}Ti_{21.5}Cr_{33.5}Zr_5$ alloy. Then the sample holder was cooled down to RT in order to reduce the pressure to an initial value, the whole process was considered as 1 cycle. The compressor cyclic tests as described above were performed up to 100 cycles. The data for only 10 cycles shown here for all the alloys to make it clear to the readers. Fig 4.16 (d) shows the cyclic stability of the alloys as a function of H_2 pressure in the sample holder at room temperature. As mentioned earlier in section 4.1.3.1,

the increase in pressure inside the sample holder at RT is a direct measure of remained excess gaseous hydrogen, which could not be absorbed by the material in each successive cycle. This can be used to estimate the degradation of the material. The pressure in the sample holder containing Nb substituted $V_{40}Ti_{21.5}Cr_{33.5}Nb_5$ alloy is continuously increased from 2 MPa to 4.85 MPa in first 50 cycles and then become stable up to 100 cycles. The degradation can be explained on the basis of phase separation during the cyclic test. XRD and SR-XRD profiles (Figs 4.12 (a) and (b)) suggest the existence of $VH_{0.81}$ phase which is quite stable and cannot desorb hydrogen at studied temperature range and remained in the alloy as dead hydrogen during the cycling, which causes the capacity decay in successive cycles. Once this phase is completely segregated, the capacity becomes stable which causes stable pressure after 50 cycles. In case of Fe substituted sample, the pressure in the sample holder is found to be increased continuously up to 100 cycles and reach to 7.5 MPa from 2 MPa. This suggests very low hydrogen absorption by the sample after 100 cycles, which is confirmed from PCI curve at RT after 100 cycles as shown in Fig 4.15 (d) where the maximum capacity could reach only 0.75 wt% at RT. This shows that the Fe substituted alloy undergoes a continuous degradation during cycling. Surprisingly, no phase segregation could be observed from XRD & SR-XRD

(Figs. 4.12 (c) and (d)). This behavior is in contrast to that for $V_{40}Ti_{21.5}Cr_{33.5}Nb_5$ and $V_{40}Ti_{21.5}Cr_{38.5}$ alloys, where the degradation is caused by the phase segregation and formation of stable Ti and V hydride phases. The possibility of this degradation can be associated with a different mechanism based on the stress/strain or dislocation defects development in the lattice during the compressor cycling as suggested earlier [70 - 72]. Kim et al [72] have shown an increase in the number of dislocation defects in bcc hydrides using the pair distribution function (PDF) analysis. It is suggested by them that the capacity degradation can be reduced by designing the alloys forming BCT (Body-Centered Tetragonal) structured hydrides. This can be observed very clearly in our experiments on Nb and Fe doped alloys. A BCT monohydride phase ($\sim VH_{0.81}$) is formed after cycling in the Nb doped sample, which must have reduced the formation of lattice defects during cycling, thus became stable after the initial decay of capacity due to the stable $VH_{0.81}$ formation as discussed above. On the other side, Fe doped alloy doesn't form BCT monohydride phase as evidenced from XRD and SR-XRD results (Fig. 4.12 (c) and (d)). It forms only bcc hydride phase which is quite easy to produce lattice defects in each successive cycle, thus continuing the capacity degradation. The pressure in the sample holder containing Zr substituted $V_{40}Ti_{21.5}Cr_{33.5}Zr_5$ alloy increased from

2 MPa to 4 MPa gradually in first 25 cycles and then became stable up to 100 cycles. The capacity decay in the first 25 cycles must be due to the transformation of $ZrCr_2$ laves phase to ZrV_2 phase through a tie line of $ZrCr_2$ – $Zr(Cr_{1-x}V_x)_2$ – ZrV_2 gradually as suggested from XRD and SR-XRD profiles shown in Figs 4.12 (e) and (f). Since cubic $ZrCr_2$ phase can absorb a high amount of hydrogen (4 H/f.u.) [73], thus contribute towards the overall initial hydrogen capacity of the material, however, it forms very stable hydride and cannot desorb hydrogen easily. Moreover, gradually formed ZrV_2 phase forms even more stable hydride [74], thus the hydride of all these materials i.e. $ZrCr_2$ – $Zr(Cr_{1-x}V_x)_2$ – ZrV_2 act as dead mass and lower the overall capacity of the material.

Fig 4.17 shows the van't Hoff plot for the parent and Nb, Zr substituted pristine alloys which are used to obtain the thermodynamic parameters i.e. enthalpy (ΔH) and entropy (ΔS) changes. The enthalpy and entropy values for Fe substituted $V_{40}Ti_{21.5}Cr_{33.5}Fe_5$ alloy could not be calculated as no plateau region appears at high temperatures (Fig 4.15 c). The enthalpy and entropy values are found to be -47 kJ mol^{-1} and 147 J mol^{-1} H$_2$ for $V_{40}Ti_{21.5}Cr_{33.5}Nb_5$ alloy and -53 kJ mol^{-1} and 159 J mol^{-1} H$_2$ for $V_{40}Ti_{21.5}Cr_{33.5}Zr_5$ alloy in comparison to the enthalpy and entropy values -41 kJ mol^{-1} and 146 J mol^{-1} H$_2$ of parent

$V_{40}Ti_{21.5}Cr_{38.5}$ alloy. The higher enthalpy value indicates the lower dissociation pressure, higher stability of the hydride and higher dehydrogenation temperature. The higher entropy value indicates a higher disorder of H_2 in the host lattice.
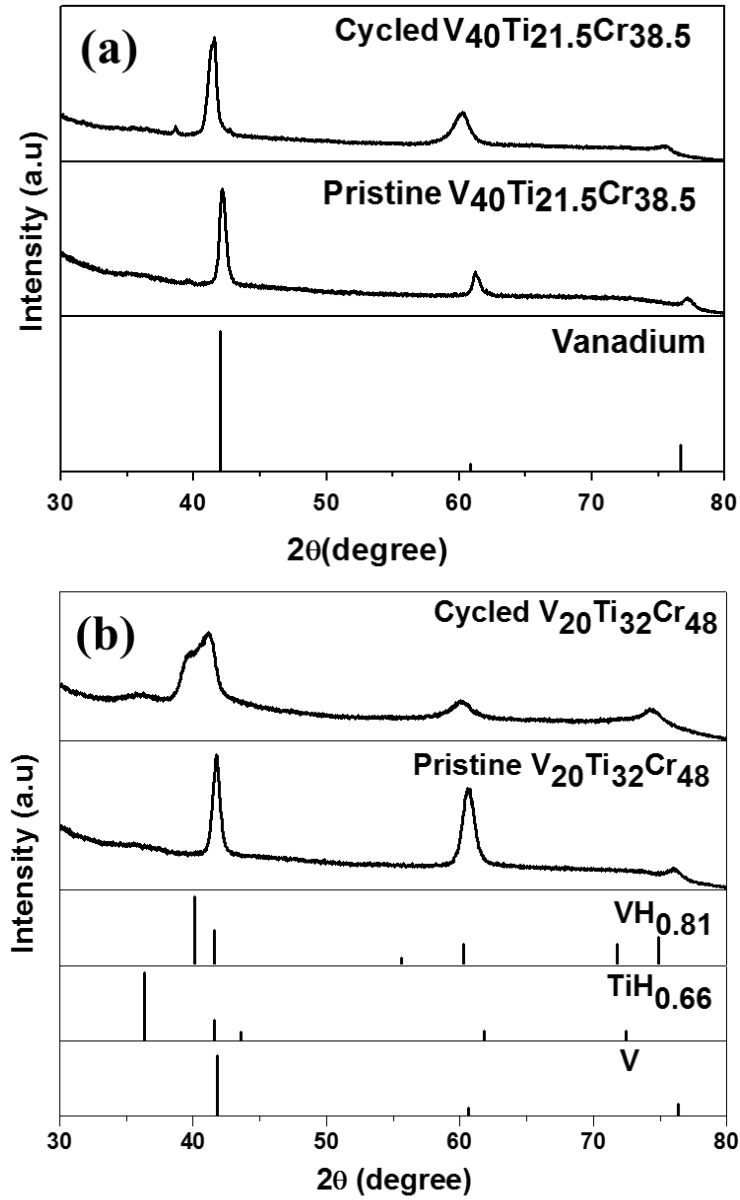
Figures

Figure 4.1: XRD profile for Pristine and cycled (a) $V_{40}Ti_{21.5}Cr_{38.5}$, (b) $V_{20}Ti_{32}Cr_{48}$ alloys. The bottom panels show the XRD peak positions corresponding to the different phases from the PDXL database.
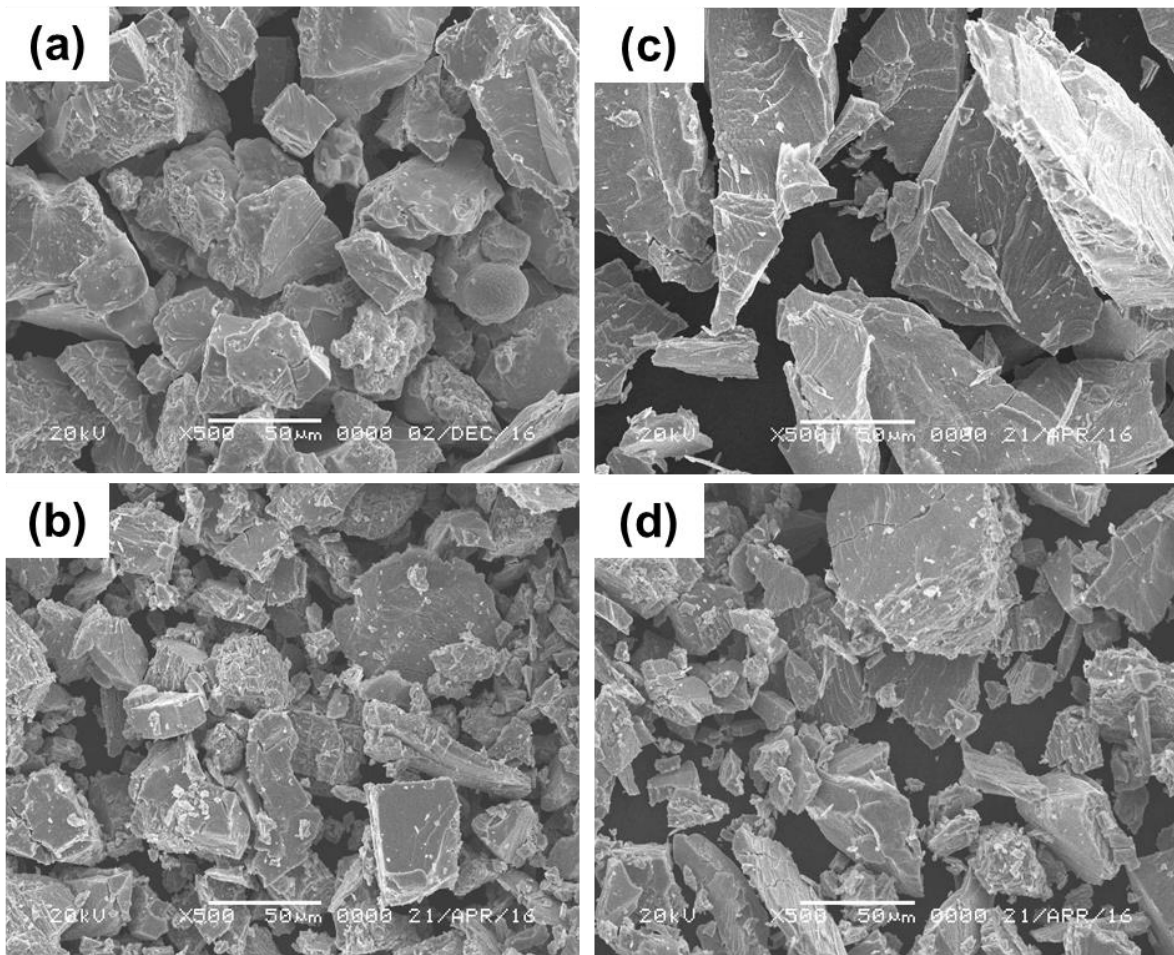
Figure 4.2: SEM morphology of (a) pristine & (b) cycled $V_{40}Ti_{21.5}Cr_{38.5}$; (c) pristine & (d) cycled $V_{20}Ti_{32}Cr_{48}$

(a)

Pt. No.	V	Ti	Cr
1	39.41	22.83	37.76
2	40.47	21.89	37.64
3	39.03	23.04	37.93
4	39.45	22.84	37.71

(b)

Pt. No.	V	Ti	Cr
1	40.53	21.22	38.25
2	39.25	22.60	38.15
3	38.74	23.49	37.78
4	40.83	20.29	38.87

(c)

Pt. No.	V	Ti	Cr
1	20.35	32.44	47.21
2	20.26	32.79	46.95
3	20.15	32.53	47.32
4	20.03	33.42	46.55

(d)

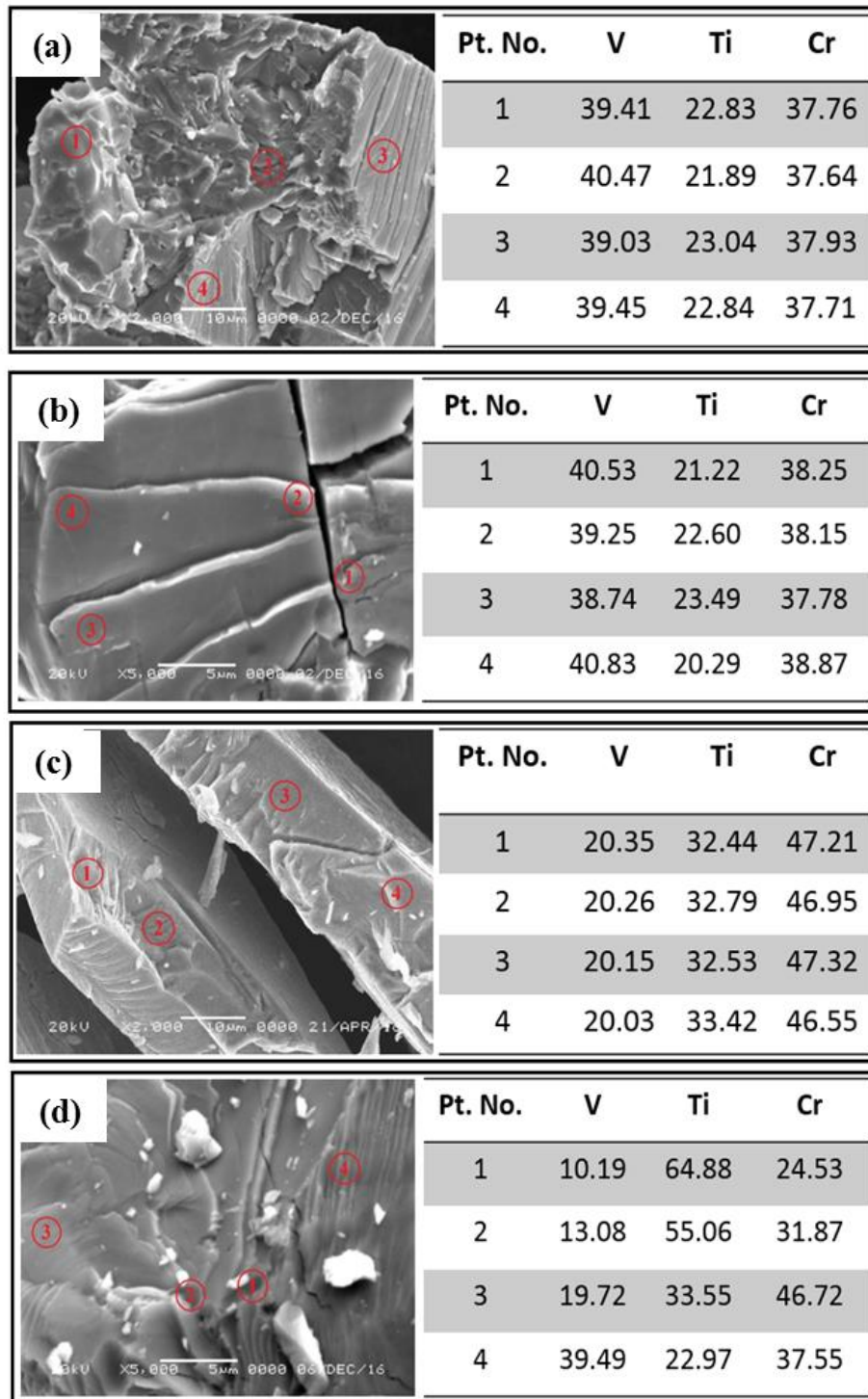| Pt. No.	V	Ti	Cr
1	10.19	64.88	24.53
2	13.08	55.06	31.87
3	19.72	33.55	46.72
4	39.49	22.97	37.55

Figure 4.3: EDS at higher magnification and the atomic percentage of the elements at different positions for (a) Pristine & (b) cycled $V_{40}Ti_{21.5}Cr_{38.5}$ alloy; (c) Pristine & (d) cycled $V_{20}Ti_{32}Cr_{48}$ alloys
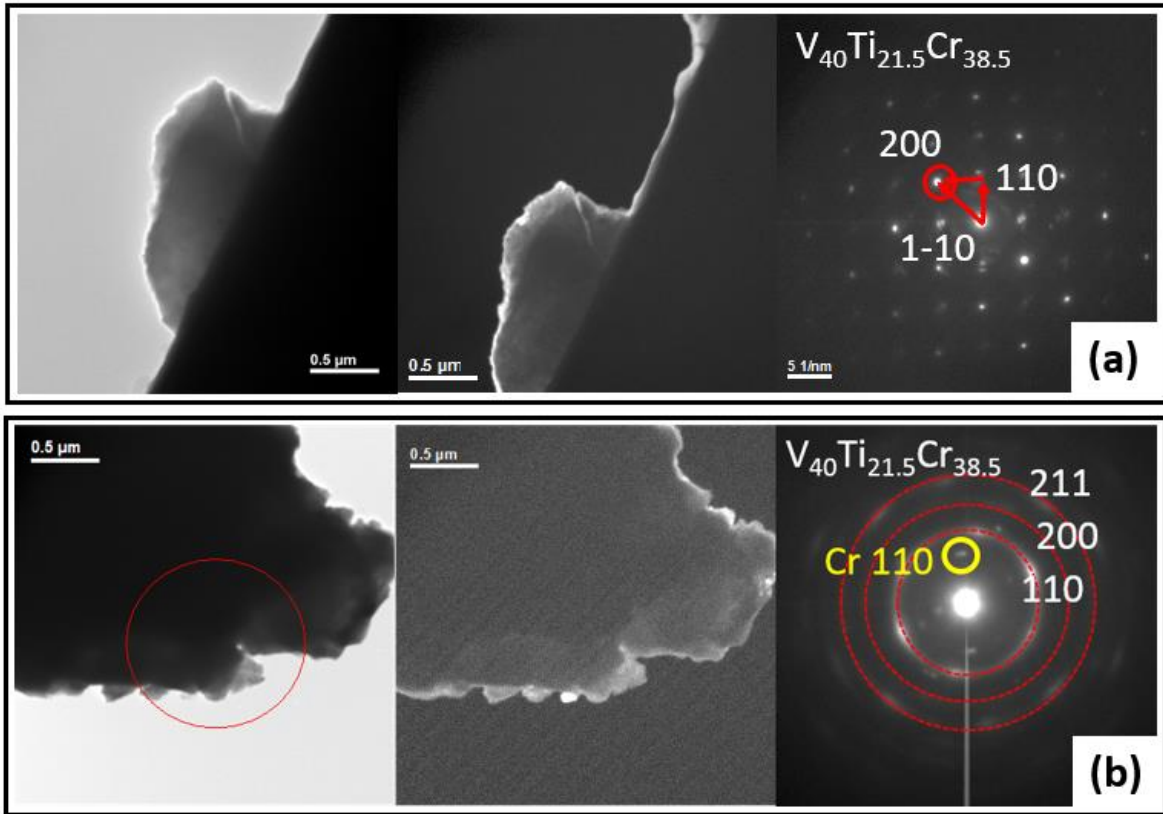
Figure 4.4: Bright Field, Dark Field images and corresponding SAED pattern for (a) Pristine and (b) Cycled $V_{40}Ti_{21.5}Cr_{38.5}$ alloys
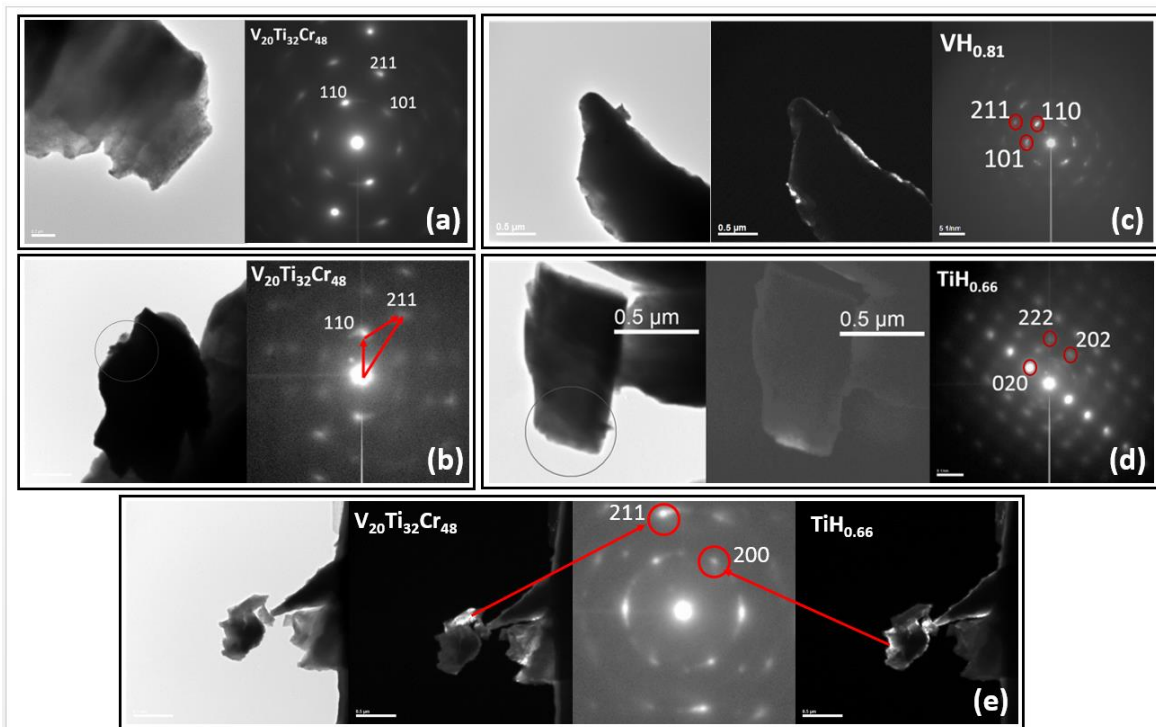
Figure 4.5: Bright Field, Dark Field images and corresponding SAED pattern for (a) Pristine and (b) – (e) Cycled $V_{20}Ti_{32}Cr_{48}$ alloys
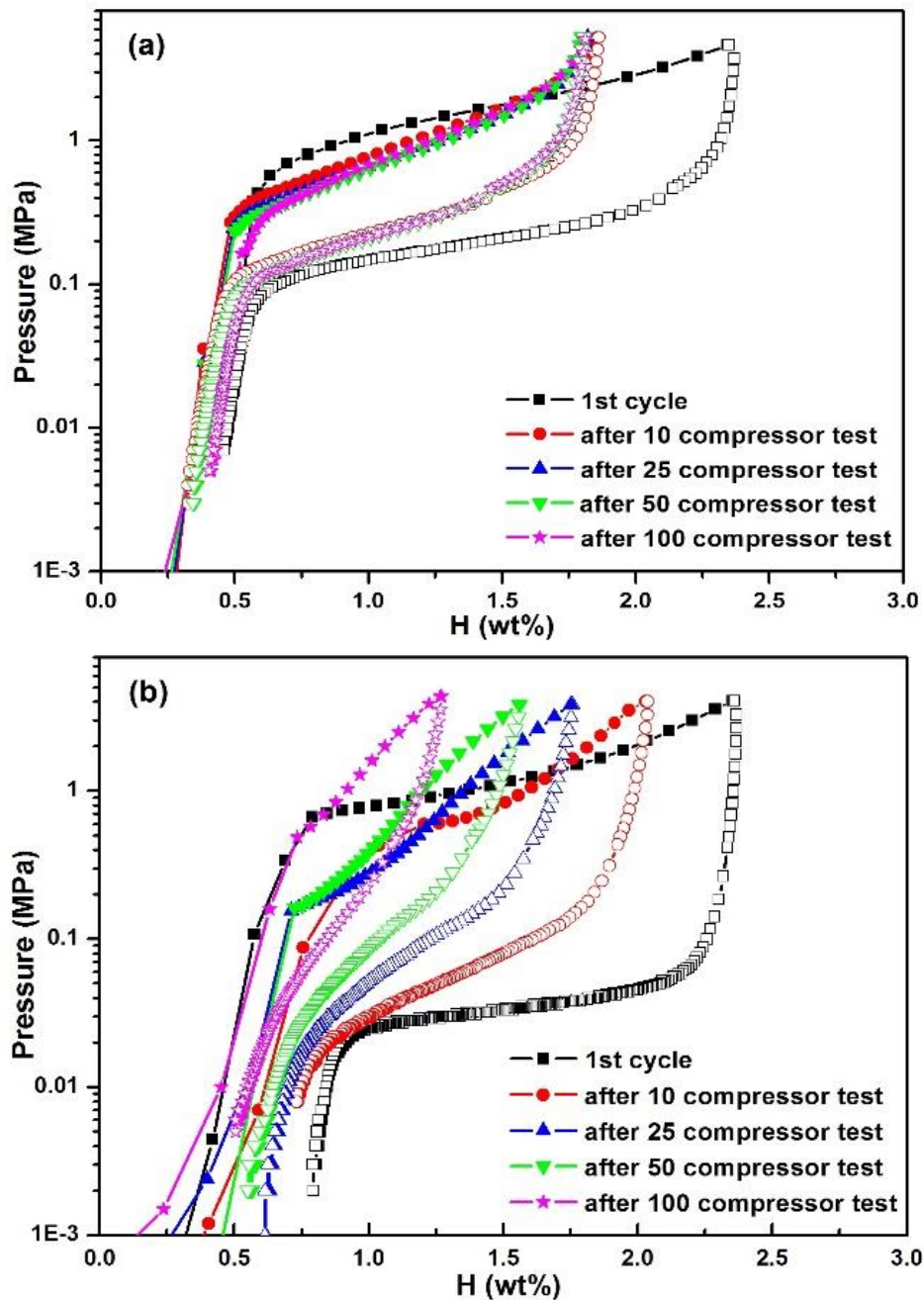
Figure 4.6: PCI curves at RT (~22°C) for (a) $V_{40}Ti_{21.5}Cr_{38.5}$, (b) $V_{20}Ti_{32}Cr_{48}$ after different cycles of compressor test. Closed symbols: Absorption, Open symbols: Desorption.
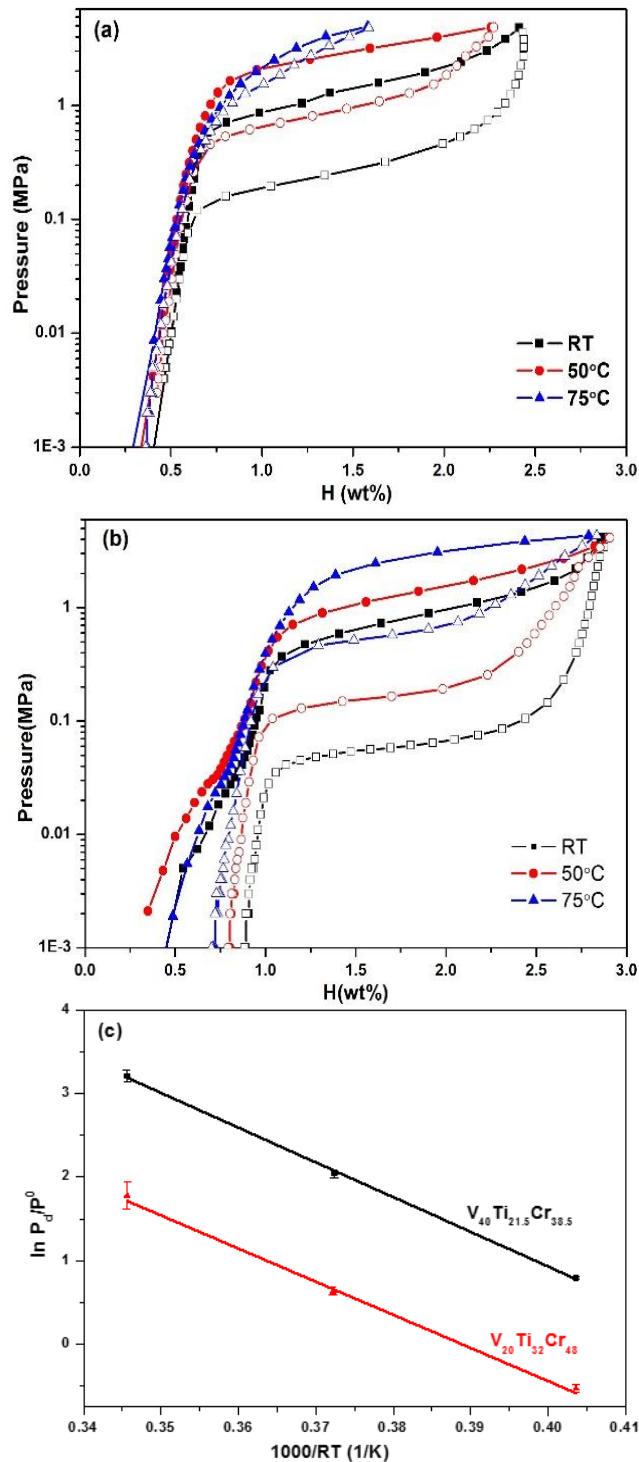
Figure 4.7: PCT curves for (a) Pristine $V_{40}Ti_{21.5}Cr_{38.5}$, (b) Pristine $V_{20}Ti_{32}Cr_{48}$; Closed symbols: Absorption, Open symbols: Desorption. (c) van't Hoff plot for both pristine alloys.
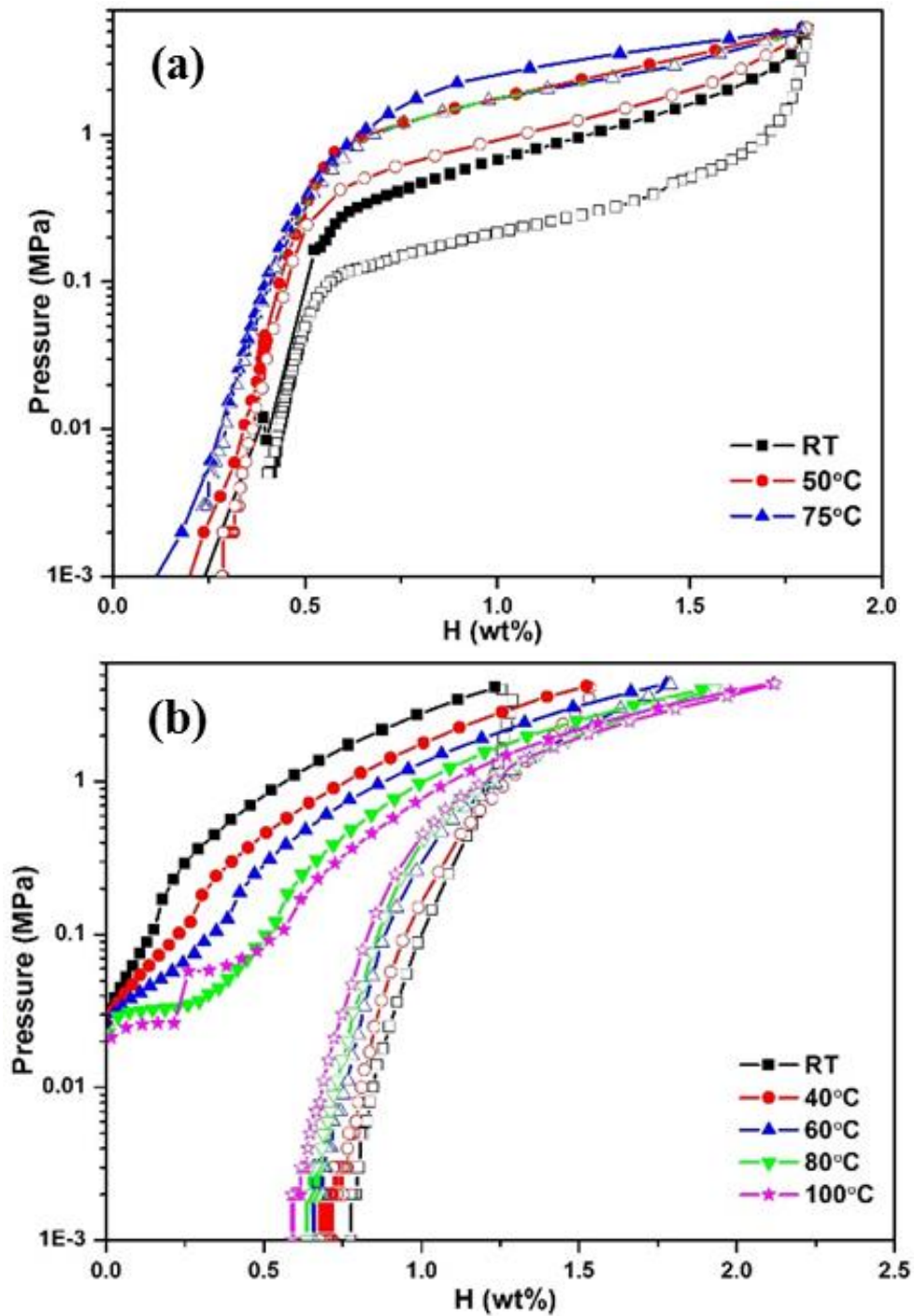
Figure 4.8: PCT curves at different temperatures for (a) Cycled V$_{40}$Ti$_{21.5}$Cr$_{38.5}$, (b) Cycled V$_{20}$Ti$_{32}$Cr$_{48}$; Closed symbols: Absorption, Open symbols: Desorption.
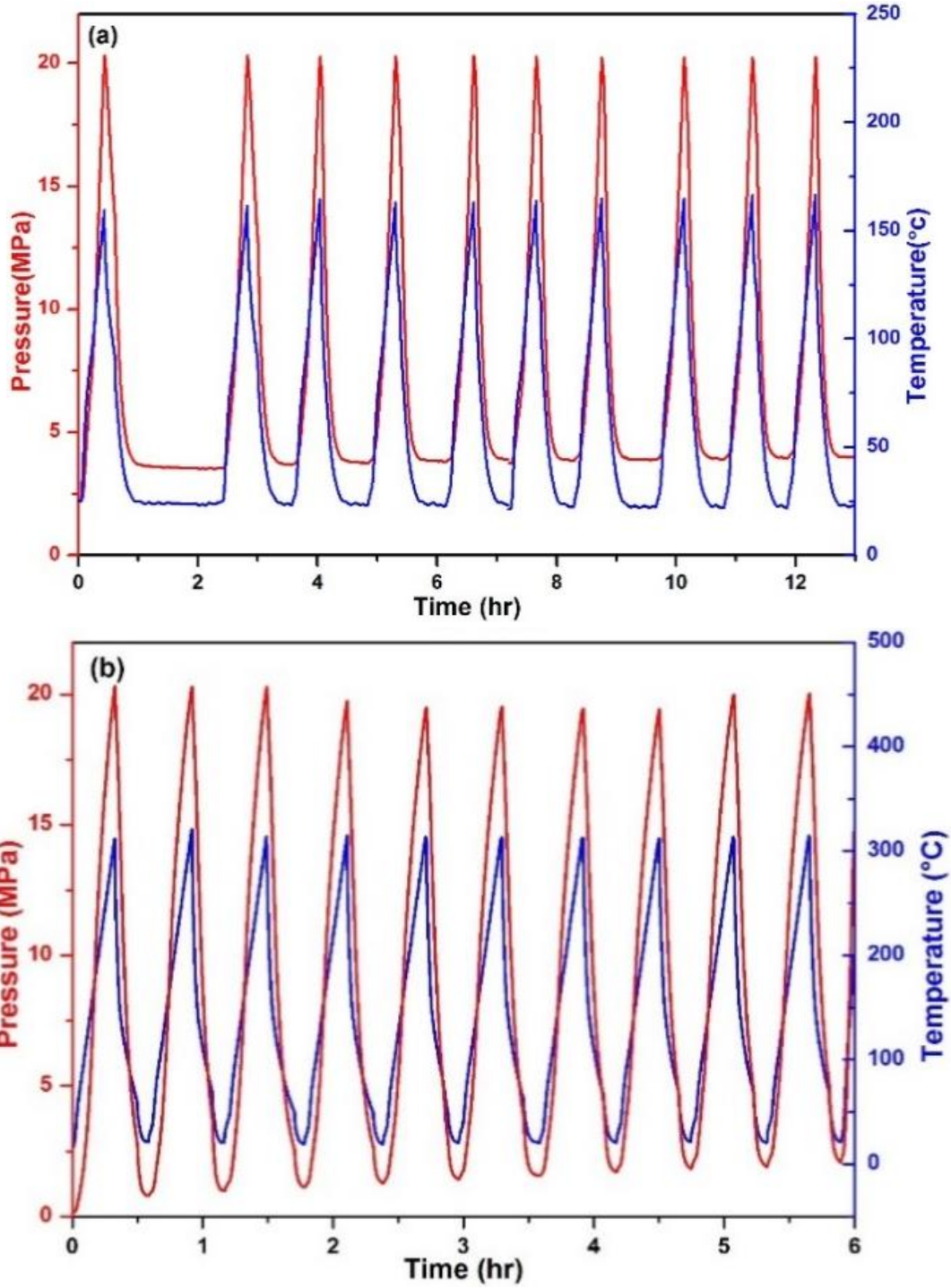
Figure 4.9: Cyclic compressor tests of (a) $V_{40}Ti_{21.5}Cr_{38.5}$ and (b) $V_{20}Ti_{32}Cr_{48}$ alloys.
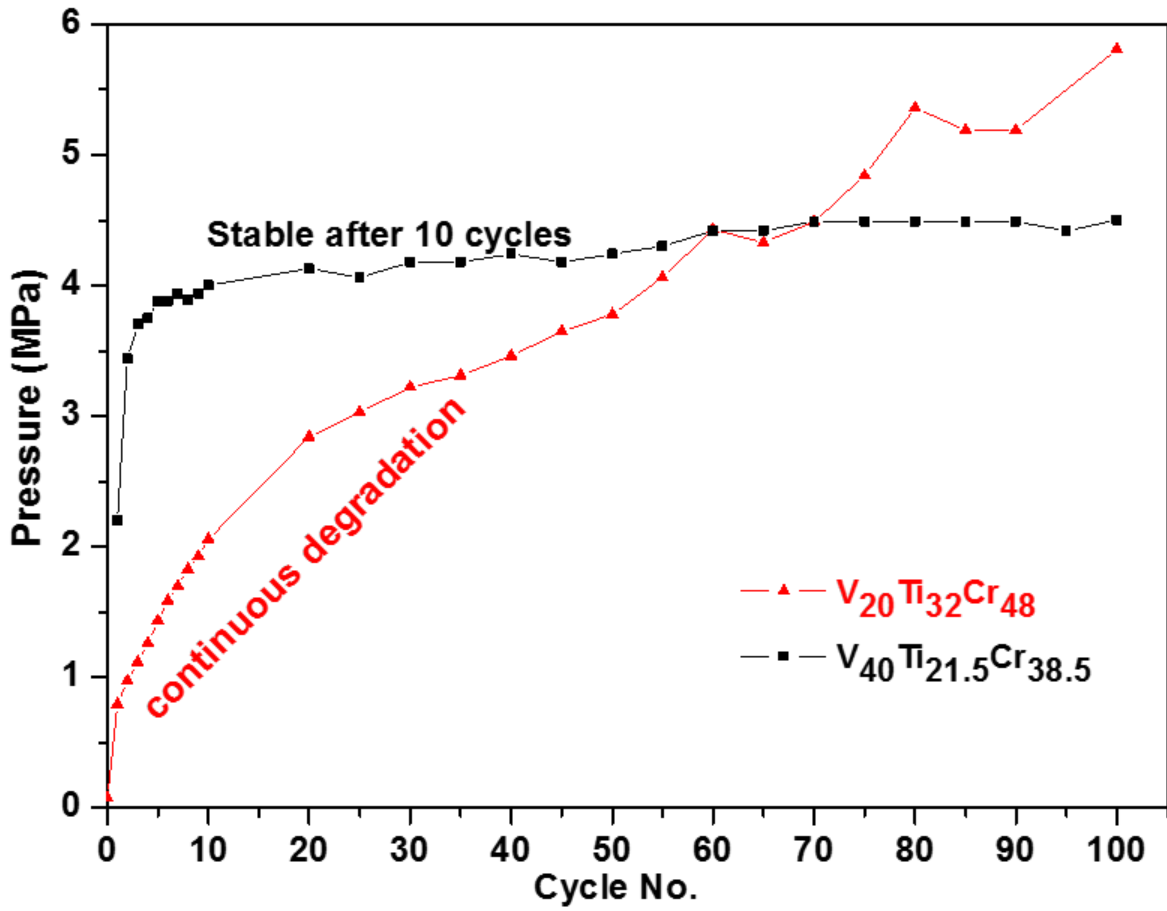
Figure 4.10: Performance comparison of both alloys in terms of system pressure variation with no. of cycles.
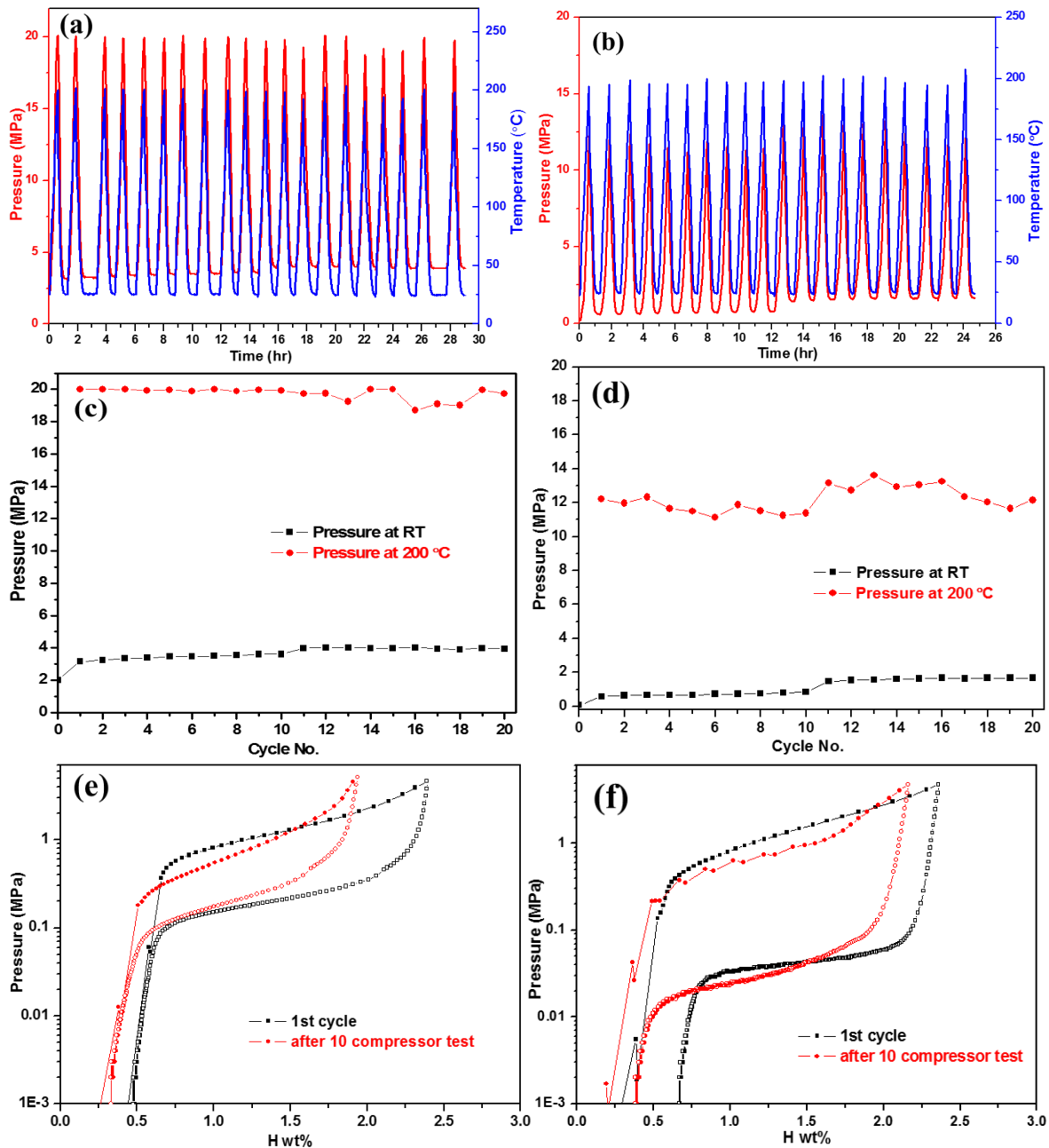
Figure 4.11: Constant temperature compressor cyclic test for $V_{40}Ti_{21.5}Cr_{38.5}$ (left) and $V_{20}Ti_{32}Cr_{48}$ (right) alloys; (a),(b) compressor cyclic test, (c),(d) pressure variation with no. of cycles, (e),(f) PCI at RT.

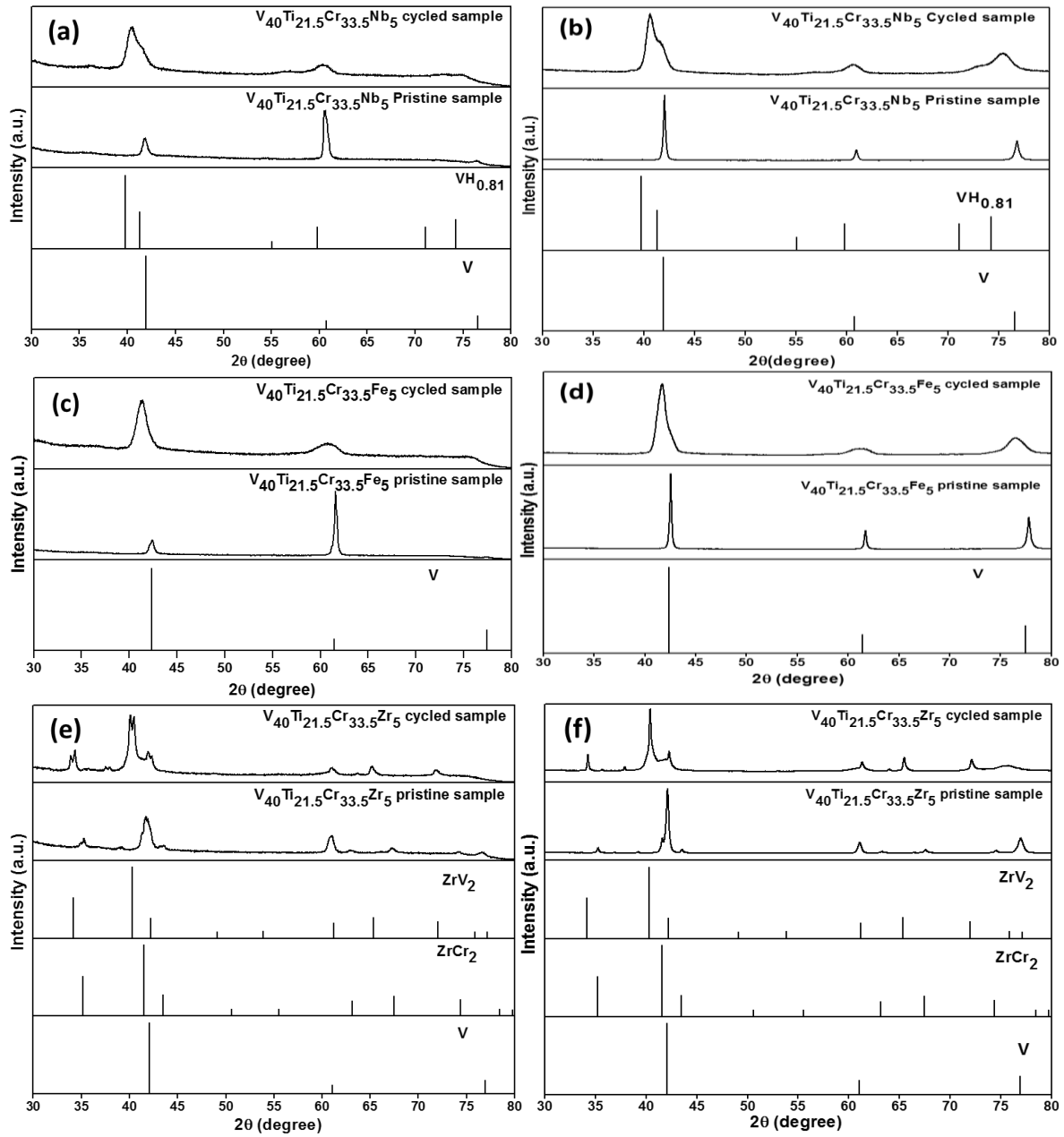**Figure 4.12: XRD (left) and SR-XRD (right) profile for Pristine and cycled (a) and (b) $V_{40}Ti_{21.5}Cr_{33.5}Nb_5$; (c) and (d) for $V_{40}Ti_{21.5}Cr_{33.5}Fe_5$; (e) and (f) for $V_{40}Ti_{21.5}Cr_{33.5}Zr_5$.**

Figure 4.13: SEM morphology for Pristine (left) and cycled (right) (a) and (b) $V_{40}Ti_{21.5}Cr_{33.5}Nb_5$; (c) and (d) $V_{40}Ti_{21.5}Cr_{33.5}Fe_5$; (e) and (f) $V_{40}Ti_{21.5}Cr_{33.5}Zr_5$ alloys.

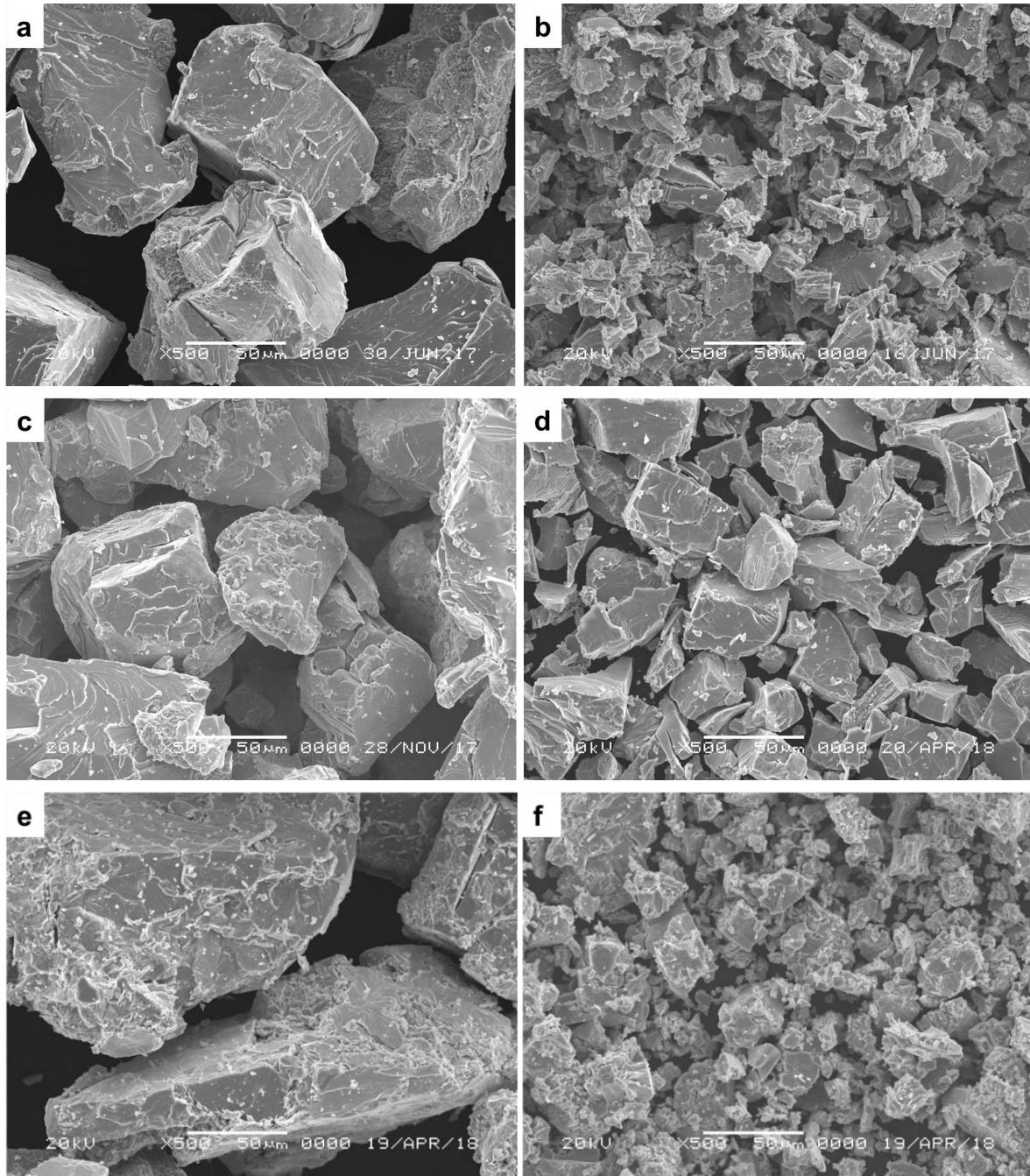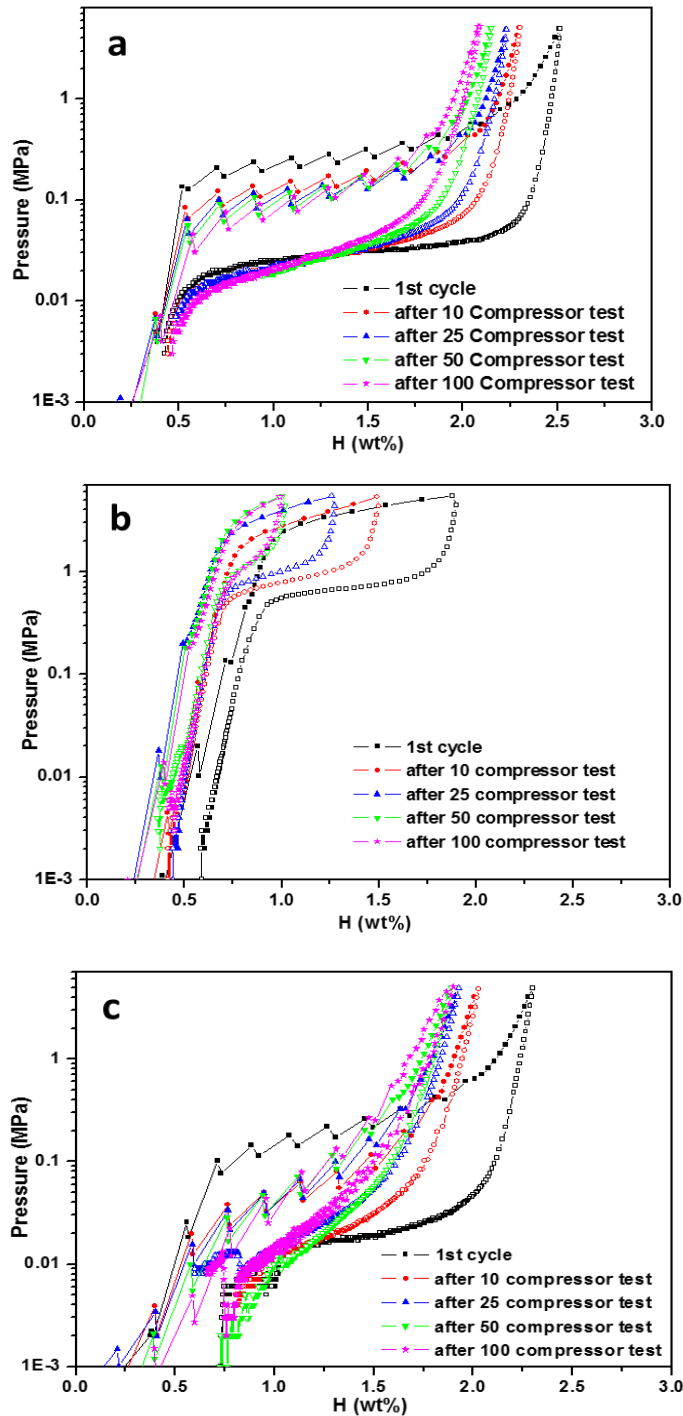**Figure 4.14: PCI curves at RT (~22°C) for (a) $V_{40}Ti_{21.5}Cr_{33.5}Nb_5$, (b) $V_{40}Ti_{21.5}Cr_{33.5}Fe_5$, (c) $V_{40}Ti_{21.5}Cr_{33.5}Zr_5$ after different cycles of compressor test. Closed symbols: Absorption, Open symbols: Desorption.**
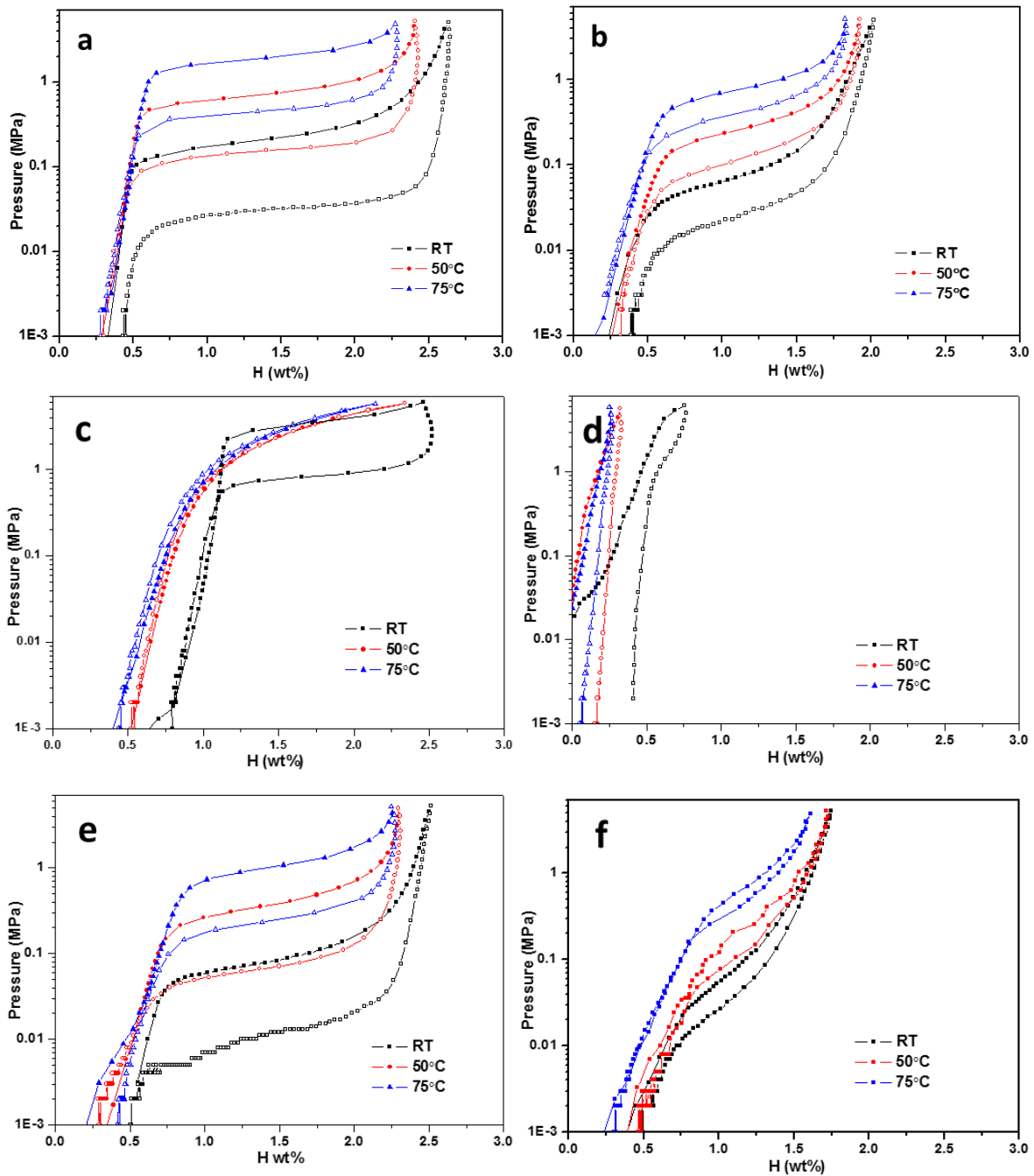
Figure 4.15: PCI curves at different temperatures for V-Ti-Cr alloys; (a),(b) pristine & Cycled $V_{40}Ti_{21.5}Cr_{33.5}Nb_5$, (c),(d) pristine &Cycled $V_{40}Ti_{21.5}Cr_{33.5}Fe_5$, (e),(f) pristine &Cycled $V_{40}Ti_{21.5}Cr_{33.5}Zr_5$; Closed symbols: Absorption, Open symbols: Desorption.

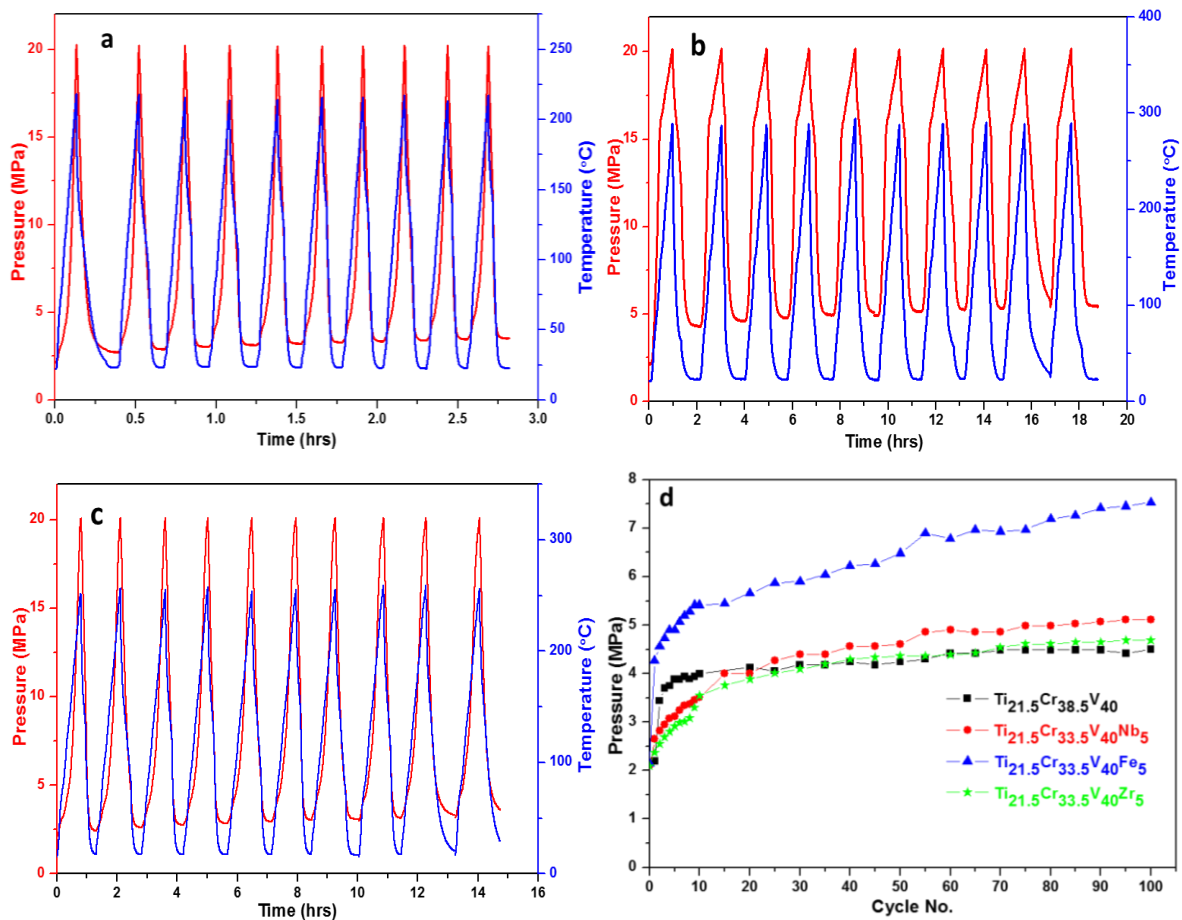**Figure 4.16: Cyclic compressor tests of (a) $V_{40}Ti_{21.5}Cr_{33.5}Nb_5$, (b) $V_{40}Ti_{21.5}Cr_{33.5}Fe_5$, (c) $V_{40}Ti_{21.5}Cr_{33.5}Zr_5$ alloys; (d) performance comparison of all alloys in terms of system pressure variation with no. of cycles.**
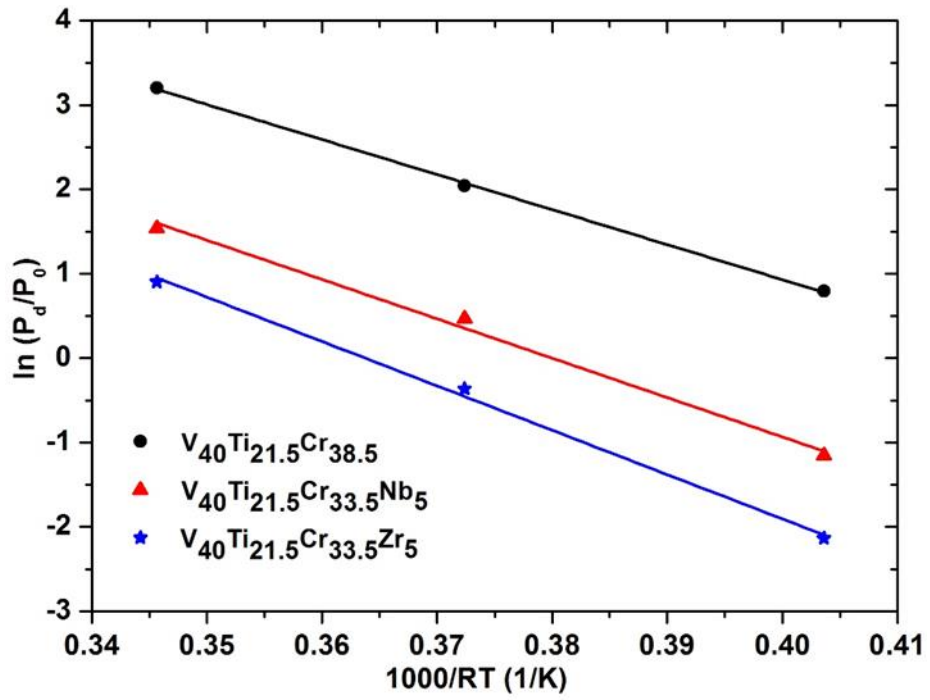
Figure 4.17: van't Hoff plot for pristine alloys

5. Conclusions

This thesis is focused on the BCC structured hydrogen storage alloys used for chemical hydrogen compressor. The hydrogen storage properties and the compressor cyclic performance for V-Ti-Cr BCC alloys were systematically investigated by the several experiments in order to understand the effect of high temperature and pressure conditions on their sorption performance.

Initially, the two different compositions V-Ti-Cr BCC alloys, namely $V_{20}Ti_{32}Cr_{48}$ and $V_{40}Ti_{21.5}Cr_{38.5}$ alloys were selected according to their effective hydrogen storage performance. The hydrogen absorption and desorption capacity of the $V_{40}Ti_{21.5}Cr_{38.5}$ alloy were found stable after 10 cycles with the plateau pressures and hysteresis remained similar up to 100 cycles while $V_{20}Ti_{32}Cr_{48}$ alloy was found to be degraded continuously over a number of cycles and hydrogen storage capacity was found to be decreased after every successive cycle. Structural and morphological investigations suggest that the low V content alloy have $TiH_{0.66}$ and $VH_{0.81}$ phases after compressor cycling. This finding suggests the low vanadium containing alloy disproportionates and a small amount of Ti and V precipitated in each hydrogenation and dehydrogenation cycle, which forms their respective hydrides during

hydrogenation. These two hydride phases are highly stable which required more than 400 °C to desorb hydrogen completely. Thus, microstructural inhomogeneity leads to stable hydride phase which seems to be the responsible reason for the gradual decrease in hydrogen storage capacity of the $V_{20}Ti_{32}Cr_{48}$ alloy in each cycle.

In order to improve the cyclic and hydrogen storage properties of $V_{40}Ti_{21.5}Cr_{38.5}$ alloy further, the fourth element i.e. Niobium (Nb), Iron (Fe), and Zirconium (Zr) have been substituted for Cr. These elements have shown their promises to alter the thermal stability as well as the cyclic performance of V-Ti-Cr ternary alloy at moderate conditions, however, no report examined the effect of high temperature and pressure conditions on the sorption performance of these substituted alloys. The compressor cyclic test for $V_{40}Ti_{21.5}Cr_{33.5}Nb_5$ alloy was found to be stable after 50 cycles with a higher hydrogen absorption and reversible capacity than that of parent and other two alloys. Structural and morphological investigations suggest the formation of $VH_{0.81}$ phase responsible for initial capacity decay for Nb substituted alloy which could not desorb hydrogen at the studied temperature range. On the other hand, $V_{40}Ti_{21.5}Cr_{33.5}Fe_5$ alloy was found to be degraded continuously over a number of cycles and hydrogen storage capacity was found to be decreased after every cycling. It is

in contrast to the earlier reports which suggest enhanced stability at room temperature with Fe substitution. However, the phase segregation could not be observed for Fe substituted alloy, in contrast to Nb substituted $V_{40}Ti_{21.5}Cr_{33.5}Nb_5$ alloy and $V_{20}Ti_{32}Cr_{48}$ alloys, suggesting that the disproportionation is not always the reason for capacity fading of these BCC alloys. The stress/strain generation in the lattice due to elevated temperature and pressure conditions during cycling seems more appropriate for this degradation. The Zr doped $V_{40}Ti_{21.5}Cr_{33.5}Zr_5$ alloy was found to be stable after 25 cycles during compressor test. The hydrogen absorption and desorption capacity were found stable after 25 cycles with the plateau pressures and hysteresis remained similar up to 100 cycles. The capacity decay in the first 25 cycles must be due to the gradual transformation of $ZrCr_2$ laves phase to ZrV_2 phase through a tie line of $ZrCr_2 - Zr(Cr_{1-x}V_x)_2 - ZrV_2$.

Finally, I conclude that Nb doped alloy among all these V-Ti-Cr alloys has the best hydrogenation properties and stability towards high temperature and pressure conditions in terms of its absorption and desorption capacity and cyclic durability.

References

[1] A. Züttel, A. Borgschulte, L. Schlapbach. Hydrogen as a Future Energy Carrier (2008).

[2] New Energy and Industrial Technology Development Organization, Japan, http://www.nedo.go.jp.

[3] Report on hydrogen storage and applications other than transportation, Government of India, New Delhi, June (2016).

[4] Energy Efficiency and Renewable Energy, Alternative Fuels Data Center, U.S Department of Energy, April 19 (2017).

[5] Secondary Energy Infobook, www.NEED.org (2017).

[6] L. Schlapbach and A. Züttel, Hydrogen-storage materials for mobile applications, Nature 414 (2001) 353-358

[7] C. H. S. Brian and A. Heinzel, Materials for fuel-cell technologies, Nature 414 (2001) 345-352.

[8] D. Mori, K. Hirose, Recent challenges of hydrogen storage technologies for fuel cell vehicles. International Journal of Hydrogen Energy 34 (2009) 4569 – 4574.

[9] http://cbc.chem.arizona.edu/~salzmanr/480a/480ants/VIRIAL/virial.html

[10] J. Hu, J. Chen, S. Sundararaman, K. Chandrashekhara, W. Chernicoff, Analysis of composite hydrogen storage cylinders subjected to localized flame impingements, International Journal of Hydrogen Energy, 33 (2008) 2738-2746.

[11] V. Alcántar, S.M. Aceves, E. Ledesma, S. Ledesma, E. Aguilera, Optimization of Type 4 composite pressure vessels using genetic algorithms and simulated annealing, International Journal of Hydrogen Energy, 42 (2017) 15770-15781.

[12] D. Halm, F. Fouillen, E. Lainé, M. Gueguen, D. Bertheau, T. v. Eekelen, Composite pressure vessels for hydrogen storage in fire conditions: Fire tests and burst simulation, International Journal of Hydrogen Energy, 42 (2017) 20056-20070.

[13] A. Züttel, A. Remhof, A. Borgschulte, O. Friedrichs, Hydrogen: The future energy carrier, Phil. Trans. R. Soc. A, 368 (2010) 3329 – 3342.

[14] A. Züttel, Materials for hydrogen storage, Materials Today, 6 (2003) 24-33.

[15] A. A. Wade, Costs of Storing and Transporting Hydrogen, National Renewable Energy Laboratory 1998.

[16] M. Hirscher and B. Panella, Nanostructures with high surface area for hydrogen storage, J. Alloys Compound. 404 (2005) 399-401.

[17] W. M. Mueller, J.P. Blackledge, G. G. Libowitz. Metal hydrides (2013).

[18] B. Sakintuna, F. L.-Darkrim, M. Hirscher. Metal hydride materials for solid hydrogen storage: A review, International Journal of Hydrogen Energy, 32 (2007) 1121-1140.

[19] https://commons.wikimedia.org/wiki/File:White_periodic_table.svg

[20] K. C. Kim, A review on design strategies for metal hydrides with enhanced reaction thermodynamics for hydrogen storage applications. International Journal of Energy Research, 42 (2018) 1455-1468.

[21] S. S. Makridis, Hydrogen storage and compression. 18 June 2016.

[22] Lennard-Jones, J.E., Trans. Faraday Soc., 28 (1932) 333.

[23] T. N. Veziroglu, S. Y. Zaginaichenko, D. V. Schur, Hydrogen Materials Science and Chemistry of Carbon Nanomaterials (2006).

[24] The Phase Rule – Concise Physical Chemistry – Rogers – Wiley Online-Oct 28 (2010).

[25] L. Schlapbach, Hydrogen in Intermetallic Compounds I, Spring-Verlag, 63 (1988).

[26] L. Schlapbach, Hydrogen in Intermetallic Compounds II, Spring-Verlag, 67 (1992).

[27] A. Andreasen, Hydrogen Storage Materials with Focus on Main Group I-II Elements, (2005).

[28] M. R. Louthan, Jr., G. R. Caskey, Jr., J. A. Donovan and D. E. Rawl, Jr. Hydrogen Embrittlement of Metals, Materials Science and Engineering, 10 (1972).

[29] X. H. Wang, Y. Y. Bei, X. C. Song, G. H. Fang, S. Q. Li, C. P. Chen, Q. D. Wang, Investigation on high-pressure metal hydride hydrogen compressors, International Journal of Hydrogen Energy, 32 (2007) 4011-401.

[30] M.V. Lototskyy, V.A. Yartys, B.G. Pollet, R.C. Bowman Jr. Metal hydride hydrogen compressors: A review, International Journal of Hydrogen Energy, 39 (2014) 5818-51.

[31] R. C. Bowman, B. Fultz, Metallic Hydrides I: hydrogen storage and other gas-phase applications. MRS Bull, 27 (2002) 688 - 93.

[32] G. Sandrock, A panoramic overview of hydrogen storage alloys from a gas reaction point of view, Journal of Alloys and Compounds, 293–295 (1999) 877–888.

[33] S. Kumar, A. Jain, T. Ichikawa, Y. Kojima, G.K. Dey, Development of vanadium-based hydrogen storage material: a review. Renew Sustain Energy Rev., 72 (2017) 791-800.

[34] X. Song, P. Pei, P. Zhang and G. Chen, Effects vanadium on hydrogen storage property in Ti-V-Cr alloys. Rare Metals, 25 (2006) 374-8.

[35] H.C Lin, K.M Lin, K.C Wu, H.H Hsiung, H K Tsai. Cyclic hydrogen absorption-desorption characteristics of TiCrV and $Ti_{0.8}Cr_{1.2}V$ alloys, International Journal of Hydrogen Energy, 32 (2007) 4966-72.

[36] J.F. Lynch, J.J. Reilly, F. Millot, The absorption of hydrogen by binary vanadium-chromium alloys, J. Phys. Chem. Solids, 39 (1978) 883 – 890.

[37] S. Ono, K. Nomura, Y. Ikeda, The reaction of hydrogen with alloys of vanadium and titanium, J. Less-Common Met., 72 (1980) 159 – 165.

[38] A. Kagawa, E. Ono, T. Kusakabe, Y. Sakamoto, Absorption of hydrogen by vanadium-rich V-Ti-based alloys, J. Less-Common Met., 172 (1991) 64 – 70.

[39] M.V. Lototsky, V.A. Yartys, I.Yu. Zavaliy, Vanadium-based BCC alloys: phase-structural characteristics and hydrogen sorption properties, J. Alloys Compd., 404-406 (2005) 421 – 426.

[40] S. Kumar, N. Krishnamurthy, Variation of activation energy of hydrogen absorption of vanadium as a function of aluminum, International Journal of Hydrogen Energy, 37 (2012) 13429 – 13436.

[41] J. Matsuda, E. Akiba, Lattice defects in V–Ti BCC alloys before and after hydrogenation, J. Alloys Compd., 581 (2013) 369 – 372.

[42] S. Suwarno, J.K. Solberg, J.P. Maehlen, B. Krogh, V.A. Yartys, The effects of rapid solidification on microstructure and hydrogen sorption properties of binary BCC Ti–V alloys, J. Alloys Compd., 582 (2014) 540 – 546.

[43] V. N. Verbetsky, T. A. Zotov, A. V. Tatarintsev, E. A. Movlaev, Hydrogen sorption properties of $V_{1-x}Cr_x$ (x = 0.1–0.5) alloys, Inorg. Mater., 49 (2013) 149 – 152.

[44] V. N. Verbetsky, T. A. Zotov, E. A. Movlaev, Absorption of hydrogen by V-Mo and V-Mo-Ti alloys, Inorg. Mater.: Appl. Res., 5 (2014) 70 – 74.

[45] S. Kumar, G.P. Tiwari, N. Krishnamurthy, Tailoring the hydrogen desorption thermodynamics of V_2H by alloying additives, J. Alloys Compd., 645 (2015) S252 – S256.

[46] A. Kagawa, E. Ono, T. Kusakabe, Y. Sakamoto, Absorption of hydrogen by vanadium-rich V-Ti-based alloys, J. Less-Common Met., 172 (1991) 64 – 70.

[47] S. Challet, M. Latroche, F. Heurtaux, Hydrogenation properties and crystal structure of the single BCC $(Ti_{0.355}V_{0.645})_{100-x}M_x$ alloys with M = Mn, Fe, Co, Ni (x = 7, 14 and 21), J. Alloys Compd., 439 (2007) 294 – 301.

[48] S.-W. Cho, C.-S. Han, C.-N. Park, E. Akiba, Hydrogen storage characteristics of Ti–Zr–Cr–V alloys, J. Alloys Compd., 289 (1999) 244 – 250.

[49] J.-H. Kim, H. Lee, P. S. Lee, C.-Y. Seo, J.-Y. Lee, A study on the improvement of the cyclic durability by Cr substitution in V–Ti alloy and surface modification by the ball-milling process, J. Alloys Compd., 348 (2003) 293 – 300.

[50] M. Tsukahara, Hydrogenation properties of vanadium-based alloys with large hydrogen storage capacity. Mater. Trans., 52 (2011) 68-72.

[51] H. Itoh, H. Arashima, K. Kubo, T. Kabutomori, K. Ohnishi, Improvement of cyclic durability of BCC structured Ti-Cr-V alloys, J. Alloys Compd., 404-406 (2005) 417-20.

[52] T. Kazumi, T. Tamura, A. Kamegawa, H. Takamura, M. Okada, Effect of absorption-desorption cycles on structure and stability of protides in Ti-Cr-V alloys, Mater. Trans., 43 (2002) 2748-52.

[53] T. Tamura, T. Kazumi, , A. Kamegawa, H. Takamura, M. Okada, Protium absorption properties and protide formations of Ti-Cr-V alloys, J. Alloys Compd, 356-357 (2003) 505-9.

[54] H.C. Lina, K.M. Lin, K.C.Wu, H.H. Hsiung, H.K. Tsai, Cyclic hydrogen absorption–desorption characteristics of TiCrV and $Ti_{0.8}Cr_{1.2}V$alloys, International Journal of Hydrogen Energy, 32 (2007) 4966 – 4972.

[55] https://www.stresstech.com/en-fi/products/x-ray-diffraction equipment/x-ray-diffraction/

[56] https://en.wikipedia.org/wiki/File:Bragg_diffraction.png

[57] S. Mobilio. Introduction to synchrotron radiation. Springer-Verlag Berlin Heidelberg 2015.

[58] Holler, Skoog, Crouch. Principle of Instrumental Analysis 6th edition.

[59] https://www.bruker.com/products/x-ray-diffraction-and-elemental-analysis/handheld-xrf/how-xrf-works.html

[60] http://www.mechscience.com/transmission-electron-microscope-temelectron-microscope/

[61] Yao, H., S. Isobe, Y. Wang, N. Hashimoto and S. Ohnuki, Plastic Bag Method for Active Sample Loading into Transmission Electron Microscope, Journal of Electron Microscopy 60, (2011), 375-378.

[62] E. Willers, M. Groll, Evaluation of metal hydride machines for heat pumping and cooling applications, International Journal of Refrigeration, 22, (1999), 47-58.

[63] Jorg Kapischke, Jobst Hapke. Measurement of the pressure-composition isotherms of high temperature and low-temperature metal hydrides, Experimental Thermal and Fluid Science 18 (1998) 70-81.

[64] M.V. Lototskyy, V.A. Yartys, B.G. Pollet, R.C. Bowman Jr., Metal hydride hydrogen compressors: A review International Journal of Hydrogen Energy, 39 (2014) 5818-5851.

[65] J. J. Reilly, R. Wiswall, The higher hydride of vanadium and niobium, Inorg. Chem., 9 (1970) 1678-1682.

[66] N. Tsurui, A. Jain, H. Miyaoka, Y. Kojima, T. Ichikawa, Development of chemical compressor up to 80MPa by using Ti-Cr-Mn alloy, MH2016 abstract book, p. 299. https://mh2016.ch/wp-content/uploads/programm/all-abstracts-mh2016.pdf.

[67] C.C. Shen, H.C. Li, Cyclic hydrogenation stability of γ-hydrides for $Ti_{25}V_{35}Cr_{40}$ alloys doped with carbon, J. Alloys Compd., 648 (2015) 534-539.

[68] S.i.Towata, T. Noritake, A. Itoh, M. Aoki, K. Miwa. Cycle durability of Ti-Cr-V alloys partially substituted by Nb or Fe, J. Alloys Compd., 580 (2013) s226-s228.

[69] E. Akiba, H. Iba, Hydrogen absorption by Laves phase related BCC solid solution, Intermetallics, 6 (1998) 461-470.

[70] D. Plante, J. Andrieux, L. Laversenne, S. Miraglia, In situ X-ray diffraction study of hydrogen sorption in V-rich Ti-V-Cr bcc solid solutions, J. Alloys Compd., 648 (2015) 79-85.

[71] M. Tsukahara, Hydrogenation Properties of Vanadium-Based Alloys with Large Hydrogen Storage Capacity, Mater. Trans., 52 (2011) 68-72.

[72] H. Kim, K. Sakai, H. Ogawa, Y. Nakamura, J. Nakamura, E. Akiba, A. Machida, T. Watanuki, T. Proffen, Origin of Degradation in the Reversible Hydrogen Storage Capacity of $V_{1-x}Ti_x$ Alloys from the Atomic Pair Distribution Function Analysis, J. Phys. Chem. C, 117 (2013) 26543 – 26550.

[73] J. Bodega, J. E. Fernandez, F. Leardini, J. R. Ares, C. Sanchez, Synthesis of hexagonal C14/C15 and cubic C15 $ZrCr_2$ laves phases and

thermodynamic stability of their hydrides, J. Phy. Chem. solids, 72 (2011) 1334-1342.

[74] Y. Zhang, J. Li, T. Zhang, T. Wu, H. Kou, X. Xue, Hydrogenation thermokinetics and activation behavior of non-stoichiometric Zr-based laves alloys with enhanced hydrogen storage capacity, J. Alloys Compd., 694 (2017) 300-308.